END
DATE
FILMED
9-80
DTIC

Polytechnic Institute of New York

LEVEL

A NUMERICAL ANALYSIS OF

MUZZLE BLAST-PRECURSOR FLOW

by GINO MORETTI

May 1980

Polytechnic Institute of New York
Aerodynamics Laboratories
Farmingdale, New York 11735

DTIC
ELECTE
AUG 4 1980
S D
D

POLY M/AE Report No. 80-10

80 8 1 052

A NUMERICAL ANALYSIS OF MUZZLE BLAST PRECURSOR FLOW

GINO MORETTI

MAY 1980

POLY M/AE Report No. 80-10

1. Introduction

Improved accuracy of fire and efficient design of anti-recoil devices cannot be achieved without a detailed knowledge of the flow field in the muzzle region of a gun, in the short interval of time (of the order of a few milliseconds, at most) between the first appearance of the projectile and its exit through the precursor shock wave. Experimental techniques have evolved to a high degree of sophistication [1,19,20,21] so that a complete description of one firing can be obtained by a combination of measurements, photographs and data processing. Innovative design, however, requires a similar detailed analysis of a large number of cases, using different models; the task is too time-consuming and expensive to be accomplished experimentally. Numerical analysis seems to be a possible alternative to experiments, although results prior to the present work have not been too encouraging.

The numerical techniques used so far have been largely inadequate to the task. Certain requirements must be satisfied, indeed, viz.:

1) The geometry of the muzzle and of the projectile must be realistic,

2) The computational program must be able to handle more complicated geometries than just a muzzle and a projectile (for example, it should include deflectors of arbitrary forms),

3) The motion of the projectile must be realistic,

4) The boundary conditions at all rigid walls must be properly handled,

5) No artificial outer boundary, capable of introducing systematic numerical errors, should exist in the program,

6) Shocks should be handled as discontinuities satisfying the Rankine-Hugoniot conditions,

7) Prediction of imbedded shock formation and treatment of shock interactions should be included in the code,

8) Two different gases, having different molecular weights and different ratios of specific heats, should be considered (although their thermodynamical behavior could be assumed

- 1 -

to be that of a perfect gas),

        9) Consequently, contact discontinuities should be explicitly handled by the code,

        10) Realistic initial conditions should be used.

        Practically, none of the requirements listed above is satisfied by any of the existing codes [2-9]. By and large, most of such codes are inspired by the early work of the Los Alamos group [10-12] which has undisputed pioneering merits but, in the light of modern developments, appears to be representative of a 'brute force' approach, typified by the use of Cartesian, evenly spaced grids, rudimentary boundaries running along grid lines, simplistic treatment of boundary conditions, smearing of discontinuities and low order of accuracy of the integration schemes.

        A cursory glance at the computational grids used in the Reports cited above shows not only their inadequacy to provide appropriate resolution where needed but the unrealistic geometry of rigid walls as they result from the choice of a basic Cartesian mesh (in other words, the mesh determines the wall geometry whereas the opposite should occur in a realistic computation). In handling rigid boundaries, large use of reflective cells is made (a by-product of Cartesian grids and straight boundaries); this can be a major source of errors [13]. The outer boundaries of the computational region are generally mishandled as well. Only recently has the majority of numerical analysts accepted the fact that disturbances produced inside the computational region must be allowed to propagate outwards without reflecting on any artificial outer boundary. How to achieve such a goal in practice, however, is not quite clear yet. SAMS (the most advanced code to date and the only code which reflects a real concern for the treatment of boundary conditions) sets all gradients to zero at the outer boundaries. Such a procedure is inconsistent with the outwards physical propagation of disturbances through the boundaries. This mistake was noticed by Zoltani [14] who tried using semi-empirical mass sinks. We believe that this approach is not correct and might be responsible for some of the catastrophic oscillations which the modified SAMS code generates and which, according to Zoltani, are not smoothed by standard artificial viscosity devices. Finally, no fitting of shocks and contact discontinuities has been attempted so far; to avoid numeri-

cal instabilities, some forms of damping have to be provided, which deface the pattern of shocks and contact discontinuities, typical of the nature of the muzzle flow.

The analysis presented in this paper has been developed on a philosophy totally different from any previous approach. Instead of trying to solve the problem on the whole field of interest considered as a single computational region, and using a single, general-purpose integration technique for the equations of fluid motion over the entire area, we subdivide the region of interest into a number of subregions, the inner and outer boundaries of which are defined on physical grounds. Each region can be studied in detail; accuracy is easier to achieve and information is not lost. In addition, the analysis of each region is based on the most sophisticated and efficient numerical techniques currently available, namely, the use of conformal mappings to define computational grids, the use of the λ-scheme, the inclusion of viscous effects, and the fitting of shocks and contact discontinuities.

In the present paper, we describe the calculation from the instant of firing through the instant at which the bullet totally emerges from the barrel. The analysis is divided into three parts, originally handled by separate codes:

1) One dimensional flow inside the barrel, in front of the bullet (code name, NS14)
2) Axisymmetric flow around the muzzle, with the bullet still inside the barrel (code name, NS9), and
3) Axisymmetric flow around the muzzle during the exit of the bullet (code name, NS18).

The three codes have been combined into a single one, named NS21, which provides an uninterrupted description of the precursor phase of evolution, based solely on geometrical and internal ballistic data.

2. One-dimensional flow inside the barrel

In this calculation, the bullet is assumed to be flat-faced. This is not a major restriction, due to the scale of the ogive with respect to the length of the barrel, and to the fact that the gas near the bullet front tends to move as a rigid body. A law of motion of the bullet as a consequence of the firing of the charge is assumed from empirical data. Generally, the bullet moves with no initial acceleration; consequently, the first perturbation is just a characteristic moving into the barrel at the speed of sound of the gas at rest. Shortly thereafter, an imbedded shock forms in the perturbed region and rapidly overtakes the perturbation front. By the time the imbedded shock, which is now identified with the perturbation front and thus became the precursor shock, reaches the gun's muzzle, the flow between the shock and the bullet is almost uniform.

The calculation is performed, at every step in time, between the perturbation front and the face of the bullet. Times are counted from the instant the bullet starts moving. The calculation begins at a time, t_o, which is very small. The perturbation front is at a distance from the initial location of the bullet face equal to $a_o t_o$, where a_o is the speed of sound of the gas at rest. A number of nodes is chosen to define the flow; initially, only two intervals are considered between bullet and perturbation front; the number of intervals is doubled as the distance between bullet and perturbation front exceeds a prescribed multiple of the initial distance; the doubling is repeated over and over again, using the same criterion, until a maximum of 64 intervals is reached. If the distance decreases, provision is made for halving the number of intervals.

The length of the computational region is normalized; that is, in addition to the physical space coordinate, z, and to the physical time, t, we use the computational variables, X and T, related to z and t by

One-dimensional flow inside the barrel

$$X = (z-b)/(c-b) \quad , \quad T = t \tag{1}$$

where b and c are the z—coordinates of the bullet face and of the perturbation front, respectively.

The flow in the barrel is assumed to be inviscid. Let ρ, p, S and θ be the thermodynamical parameters density, pressure, entropy and temperature, respectively, u the velocity and t the time. Pressure and density of the gas at rest are assumed as unity; the speed of sound of the gas at rest, divided by the square root of γ, is assumed as the unity of speed. The inner radius of the barrel is assumed as the unity of length. With a suitable definition of the unity of time, as the ratio of the unity of length to the unity of speed, and letting

$$P = \ln p \quad , \quad \theta = p/\rho \tag{2}$$

$$S = \gamma \ln \theta - (\gamma-1) P \tag{3}$$

the equations of motion in the (X,T) frame are:

$$P_T + A P_X + \gamma X_z u_X = 0$$

$$u_T + A u_X + \theta P_X = 0 \tag{4}$$

$$S_T + A S_X = 0$$

where

$$A = u X_z + X_t \tag{5}$$

$$X_z = 1/(c-b) \quad , \quad X_t = X_z[(X-1)b_t - X c_t] \tag{6}$$

The equations of motion are integrated at all nodal points (including the node on the bullet and the one at the perturbation front) using the λ-scheme [15]. Special treatments are given to the boundary points and the points next to the boundaries, to avoid using information from outside the boundaries. Note that at the bullet point we need to compute the pressure only, since u coincides with the prescribed b_t and S is always equal to its initial value, assumed as zero. The pressure is,

thus, obtained by using the equation for left running characteristics:

$$P_T = -\lambda_1 P_{X1} + \frac{\gamma}{a}(b_{tt} - \lambda_1 u_{X1}) \quad , \quad \lambda_1 = A - X_z a \qquad (7)$$

At the end of the corrector level, at each time step, pressure and velocity are corrected at the perturbation front, assuming that it is a shock (obviously, in the first phase of the motion, such a shock degenerates into a characteristic). Shocks are computed using the post-correction technique [16]. In the case of a shock moving into a gas at rest with a speed $W = c_t$, we have

$$\partial P/\partial W = 2W/(W^2 - \delta) \quad , \quad \partial u_{rel}/\partial W = -\delta(\delta+1) + \gamma/[(\delta+1)W^2]$$

$$\qquad (8)$$

$$\delta = (\gamma-1)/2$$

$$P^* = \ln(W^2 - \delta) - \ln(\delta+1) \quad , \quad u_{rel}^* = -\delta/(\delta+1)W - \gamma/[(\delta+1)W] \quad (9)$$

$$\Delta W = -[a(P^* - P^{(E)}) + \gamma(u_{rel}^* + W - u^{(E)})]/[a \, \partial P/\partial W + \gamma(\partial u_{rel}/\partial W + 1)] \quad (10)$$

where $P^{(E)}$, $u^{(E)}$ are the values obtained by integrating the Euler equations. After updating W, the values behind the shock are recomputed from the Rankine-Hugoniot conditions. The location of the shock, c, is updated using

$$\Delta c = (c_t + \frac{1}{2}c_{tt}\Delta t)\Delta t = (W + \frac{1}{2}\Delta W)\Delta t \qquad (11)$$

At every computational step, the value and location of the maximum pressure gradient is monitored; when it exceeds a given tolerance (say, $\partial P/\partial z > 2$), an imbedded shock is fitted at the center of the computational mesh where the maximum gradient occurs. The interpolated local pressure is assumed to be the pressure in front of the shock. The pressure at the next node is assumed as the pressure behind the shock; and the shock Mach number, initial velocity and other pertinent values are calculated consistently.

The imbedded shock is computed in a similar way. Let W be the shock velocity and the values in front of the shock be denoted by an index, 1; then

$$u_{1rel} = u_1 - W \quad , \quad M^2_{rel} = (u_{1rel}/a_1)^2 \qquad (12)$$

$$d = \gamma M^2_{rel} - \delta$$

$$P^* = P_1 + \ln d/(\delta+1) \qquad (13)$$

$$u^*_{rel} = \delta/(\delta+1) \, u_{1rel} + a_1^2/[(\delta+1) \, u_{1rel}]$$

$$\partial P/\partial W = -2 \, u_{1rel}/(d\theta_1)$$

$$\partial u/\partial W = (M^2_{rel}+1)/(\delta+1) \qquad (14)$$

$$\Delta W = - [a(P^*-P^{(E)})+\gamma(u^*_{rel}+W-u^{(E)})]/(a \, \partial P/\partial W + \gamma \, \partial u/\partial W) \qquad (15)$$

3. Numerical results

For a numerical example, a 5.56 mm gun was chosen, fo which the bullet velocity can be defined by the following equations:

$$b_t = E \, (t/100)^5 \qquad t < t_o$$

$$b_t = At + B + 1/(Ct + D) \qquad t \geq t_o$$

with $t_o = 70$, $E=10$ and A,B,C,D defined by the conditions:

$$b_t = 1.6807 \quad , \quad b_{tt} = .12005 \quad \text{at } t=70$$

$$b_t = 3.5 \quad , \quad b_{tt} = .007 \quad \text{at } t=125$$

that is, $A=-0.0042$, $B=4.8983$, $C=-0.0145$, $D=0.6739$. The velocity of the bullet as a function of time is shown in Fig. 1. Some plots of pressure distributions are displayed in Fig. 2.

The peculiar shape of the pressure distribution at the highest value of time is due to the effect of variable entropy behind the accelerating imbedded shock.
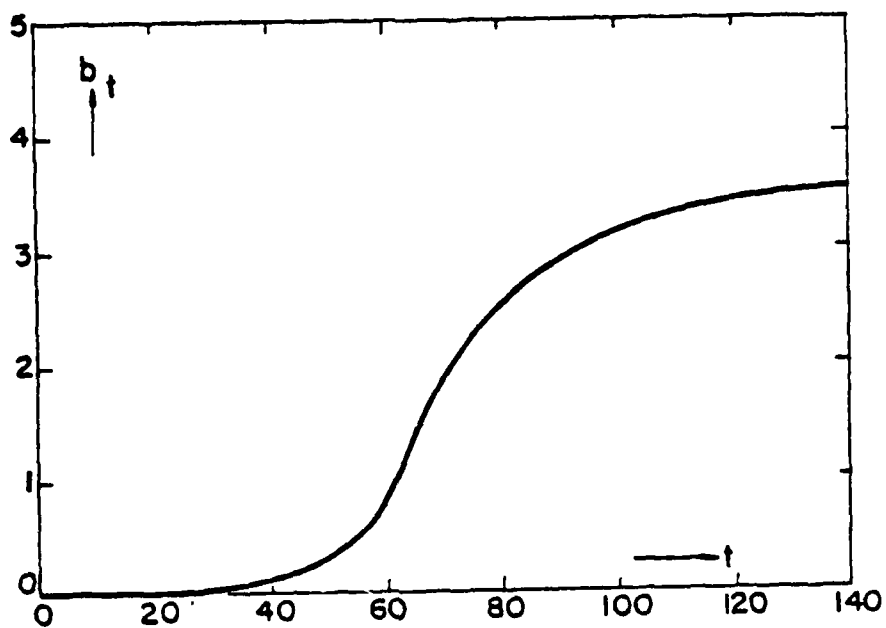
Fig. 1

Fig. 2

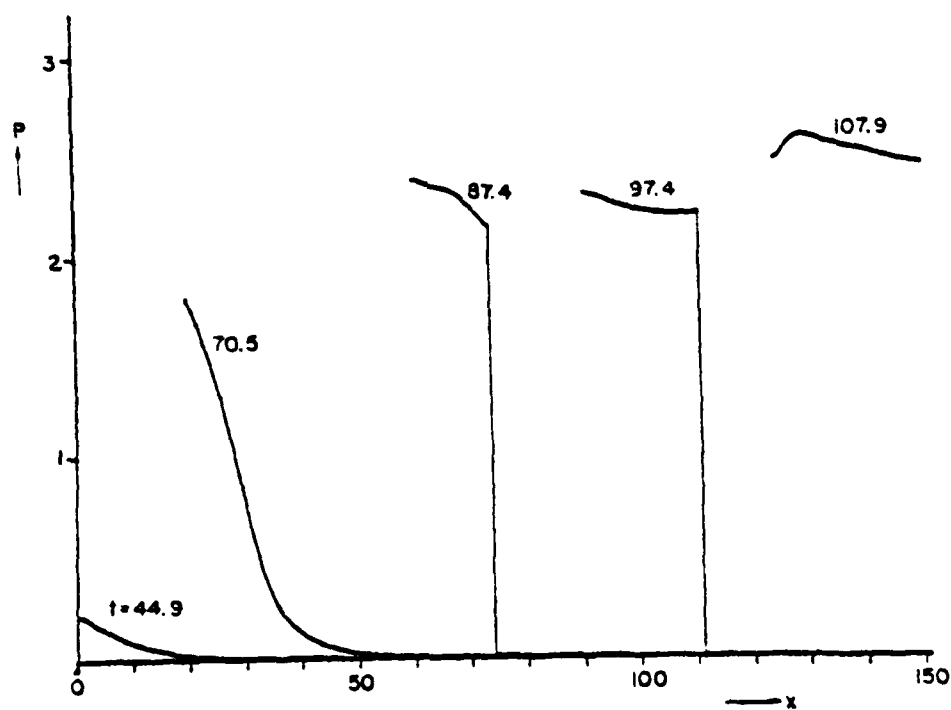## 4. First phase of precursor shock evolution

As the precursor shock reaches the mouth of the barrel, we start the calculation of the axisymmetric flow around the muzzle. Typically, the flow is limited by:

1) the centerline of the gun,
2) the precursor shock,
3) the outer wall of the gun, and
4) the mouth of the barrel.

The flow is assumed to be viscous. The inviscid flow model would be both unrealistic and numerically unmanageable; a preliminary discussion of the difficulties can be found in [18].

A detailed description of the equations of motion is given in [17], from which the part relevant to the present calculation is transcribed.

5. Equations of motion

Let $\vec{V}$ be the velocity vector, t the time, κ the coefficient of heat conduction, and Φ the dissipation term. The latter is a well-known non-negative quadratic form depending on the space derivatives of the velocity components. Its expressions for the coordinate system considered in the present paper will be given later on. We will assume that the viscosity, μ, is a constant.

A Reynolds number and a Prandtl number can be defined as

$$R_e = \rho_{ref} u_{ref} x_{ref} / \mu, \qquad P_r = c_p \mu / \kappa \qquad (16)$$

where c_p is the specific heat at constant pressure. Using the

- 9 -

same units as in section 2, the equations of motion for a viscous flow (Navier-Stokes equations) can be written in the form:

$$\frac{D\rho}{Dt} + \rho \nabla . \vec{V} = 0$$

$$\frac{D\vec{V}}{Dt} + \frac{1}{\rho} \nabla p = \frac{1}{\rho R_e} [\frac{4}{3} \nabla \nabla . \vec{V} - \nabla \times \nabla \times \vec{V}]$$

$$\frac{DS}{Dt} = \frac{1}{\rho R_e}[(\gamma-1)\Phi + \frac{\gamma}{P_r} \nabla^2 \theta]$$

(17)

In an inviscid flow, the terms here affected by $1/R_e$ do not appear. For a proper numerical analysis of such flows, whose mechanics is governed by the propagation of sound waves and by the convection of entropy along particle paths, it is convenient to recast the equations of motion into a form similar to (4):

$$\frac{DP}{Dt} + \gamma \nabla . \vec{V} = 0$$

$$\frac{D\vec{V}}{Dt} + \theta \nabla P = 0$$

$$\frac{DS}{Dt} = 0$$

(18)

If the flow is viscous, the basic phenomena of wave propagation are still present, although modified by the concurrent effects of diffusion. Therefore, it would not be advisable to drop the basic integration techniques for convective terms; we will consequently write the Navier-Stokes equations in the form:

$$\frac{\partial P}{\partial t} + \vec{V} . \nabla P + \gamma \nabla . \vec{V} = \frac{DS}{Dt}$$

$$\frac{\partial \vec{V}}{\partial t} + \frac{1}{2}\nabla(q^2) - \vec{V} \times \nabla \times \vec{V} + \theta \nabla P = \frac{1}{\rho R_e} [\frac{4}{3} \nabla \nabla . \vec{V} - \nabla \times \nabla \times \vec{V}]$$

$$\frac{\partial S}{\partial t} + \vec{V} . \nabla S = \frac{1}{\rho R_e}[(\gamma-1)\Phi + \frac{\gamma}{P_r} \nabla^2 \theta]$$

(19)

(where the material derivatives have been replaced by partial derivatives, as costumary, and q is the modulus of the velocity). In what follows, the density will no longer be used explicitly, and ρ will be redefined in Eq. (21).

6. Conformal mapping

We will consider two types of flows, both depending on two space variables: two-dimensional (plane) flows and axi-symmetric flows. Two Cartesian coordinates, x and y, will be used for two-dimensional flows. The same symbols will be used for the axial and radial coordinate, respectively, in any meridional plane of an axi-symmetric flow. The (x,y)-plane will be called the physical plane. We must provide a computational grid with a family of lines running from the centerline to the wall and another family of lines running from the mouth to the shock. To this effect, we begin by introducing a complex variable

$$z = x + i y \tag{20}$$

and assume that, in general, the physical plane will be conformally mapped onto an auxiliary plane, described in terms of a complex variable ζ,

$$\zeta = \rho \, e^{i\theta} \tag{21}$$

Such a mapping is:

$$z = (r_o/\pi)[(z_1^2 - 1/z_1^2)/2 - \log z_1^2 - i\pi] \tag{22}$$

$$z_1 + 1/z_1 = 2B \, (\zeta + 1/\zeta)$$

where r_o is the outer radius of the barrel, and B is determined to assure correspondence between $\zeta=1$ and $z = -i$. Lines of constant ρ and of constant θ in the ζ-plane are mapped onto the grid shown in Fig. 3. If a θ = constant line, different from BD (for example, FG), is used as a boundary, the flow in the physical plane will occur in the divergent duct having FG as a wall. Let
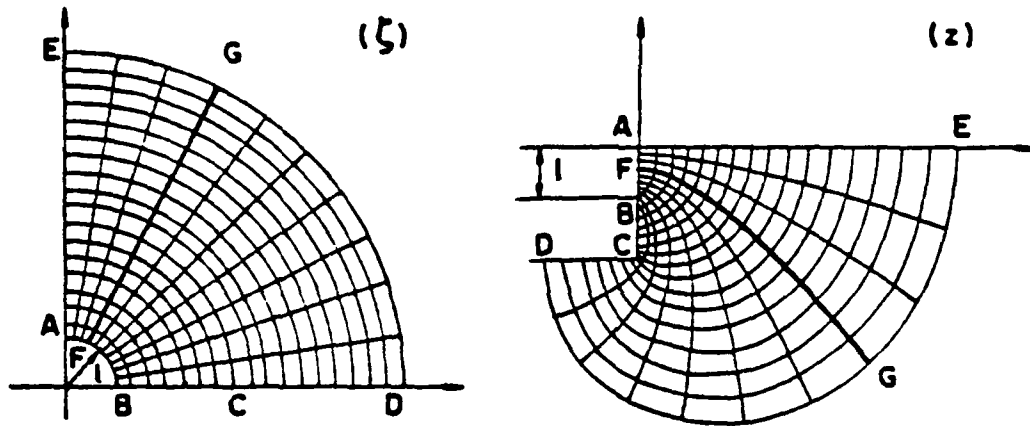
$$g = \frac{d\zeta}{dz} = Ge^{i\omega} \tag{23}$$

Fig. 3

$$z + i\mathcal{S} = \frac{G\zeta}{\rho g} = e^{i(\theta - \omega)} \tag{24}$$

$$z = \cos(\theta - \omega) \ , \quad \mathcal{S} = \sin(\theta - \omega) \tag{25}$$

$$\phi = \frac{\zeta}{g} \frac{d \log g}{dz} = \phi_1 + i\phi_2 \tag{26}$$

Let also $\hat{\imath}$, $\hat{\jmath}$ be the unit vectors tangent to the θ = constant line and to the ρ = constant line in the z-plane, and u and v be the corresponding velocity components, respectively, so that

$$\vec{V} = u \, \hat{\imath} + v \, \hat{\jmath} \tag{27}$$

It is convenient to note that

$$\rho_x = Gz, \quad \rho_y = G\mathcal{S}, \quad \theta_x = -\frac{G}{\rho} \mathcal{S}, \quad \theta_y = \frac{G}{\rho} z \tag{28}$$

$$x_\rho = z/G, \quad x_\theta = -\rho\mathcal{S}/G, \quad y_\rho = \mathcal{S}/G, \quad y_\theta = \rho z/G \tag{29}$$

$$\rho_x^2 + \rho_y^2 = G^2 \ , \quad x_\rho^2 + x_\theta^2/\rho^2 = 1/G^2 \tag{30}$$

$$G_\rho = G\phi_1/\rho \ , \quad G_\theta = -G\phi_2 \ , \quad \omega_\rho = \phi_2/\rho \ , \quad \omega_\theta = \phi_1, \tag{31}$$

- 12 -

If $\hat{I}$ and $\hat{J}$ are the unit vectors parallel to the x- and y-axis, respectively, and

$$\vec{V} = U \; \hat{I} + V \; \hat{J} \tag{32}$$

it follows that

$$\hat{I}.\hat{I}=\mathcal{C} \;, \quad \hat{I}.\hat{J}=\mathcal{S} \;, \quad \hat{J}.\hat{I}=-\mathcal{S} \;, \quad \hat{J}.\hat{J}=\mathcal{C} \tag{33}$$

$$U=u\mathcal{C}-v\mathcal{S}, \quad V=u\mathcal{S}+v\mathcal{C}, \quad u=U\mathcal{C}+V\mathcal{S}, \quad v=-U\mathcal{S}+V\mathcal{C} \tag{34}$$

For any element ds $\underline{in \; space}$, we have

$$ds^2 = \frac{1}{G^2}d\rho^2 + \frac{\rho^2}{G^2} \; d\theta^2 + jy^2 dx_3^2 \tag{35}$$

if x_3 is the angular coordinate in an axi-symmetric problem and j is a multiplier, equal to 0 for two-dimensional flows and to 1 for axi-symmetric flows. Consequently, the basic vector operators in (19) can be expressed as follows:

$$\nabla P = G(P_\rho \hat{I} + \frac{1}{\rho} \; P_\theta \hat{J}) \tag{36}$$

$$\nabla \times \vec{V} = \frac{G^2}{\rho}[\; (\frac{\rho v}{G})_\rho - (\frac{u}{G})_\theta] \tag{37}$$

$$\vec{V} \times \nabla \times \vec{V} = \frac{G^2}{\rho}[\; (\frac{\rho v}{G})_\rho - (\frac{u}{G})_\theta](v\hat{I}-u\hat{J}) \tag{38}$$

$$\nabla.\vec{V} = \frac{G^2}{\rho}[\; (\frac{\rho u}{G})_\rho + (\frac{v}{G})_\theta] + j \; \frac{V}{y} \tag{39}$$

and

$$\Phi = 4(e_{12}^2+e_{23}^2+e_{31}^2) + \frac{2}{3}[(e_{11}-e_{22})^2+(e_{22}-e_{33})^2+(e_{33}-e_{11})^2] \tag{40}$$

with

$$e_{11} = G(u_\rho + \frac{v}{\rho} \; \phi_2) \;, \quad e_{22} = \frac{G}{\rho}[v_\theta + u(1-\phi_1)] \;, \quad e_{33} = j \; \frac{V}{y}$$

- 13 -

$$e_{12} = \frac{1}{2}G[v_\rho - \frac{v}{\rho}(1-\phi_1) + \frac{1}{\rho}(u_\theta - u\phi_2)] \tag{41}$$

and e_{33}, e_{23}, e_{31} equal to zero. We will denote by Ω the only non-zero component of the curl of $\vec{V}$ (37):

$$\Omega = G(v_\rho - \frac{1}{\rho}u_\theta) - D \tag{42}$$

and by Δ the divergence of $\vec{V}$ (39):

$$\Delta = e_{11} + e_{22} + e_{33} \tag{43}$$

and introduce the symbols

$$D = \frac{G}{\rho}[-v(1-\phi_1) + u\phi_2] \tag{44}$$

$$E = \frac{G}{\rho}[u(1-\phi_1) + v\phi_2] + e_{33} \tag{45}$$

It is easy to see that, in terms of the independent variables ρ and θ, the Navier-Stokes equations are:

$$P_t + G(uP_\rho + \frac{v}{\rho}P_\theta) + \gamma G(u_\rho + \frac{v_\theta}{\rho}) + \gamma E = \frac{DS}{Dt}$$

$$u_t + G(uu_\rho + \frac{v}{\rho}u_\theta) + vD + G\theta P_\rho = (\frac{4}{3}G\Delta_\rho - \frac{G}{\rho}\Omega_\theta - j\frac{\ell}{y}\Omega)\frac{\theta}{pR_e}$$

$$\tag{46}$$

$$v_t + G(uv_\rho + \frac{v}{\rho}v_\theta) - uD + \frac{G}{\rho}\theta P_\theta = (\frac{4}{3}\frac{G}{\rho}\Delta_\theta + G\Omega_\rho + j\frac{3}{y}\Omega)\frac{\theta}{pR_e}$$

$$S_t + G(uS_\rho + \frac{v}{\rho}S_\theta) = [(\gamma-1)\Phi + \frac{\gamma}{P_r}\nabla^2\theta]/(pR_e)$$

with Φ defined by (40) and

$$\nabla^2\theta = \frac{G^2}{\rho}(\theta_\rho + \rho\theta_{\rho\rho} + \frac{1}{\rho}\theta_{\theta\theta}) + jG\frac{\theta_\rho 3 + \theta_\theta \ell/\rho}{y} \tag{47}$$

7. Computational plane

The ζ-plane, however, is not the computational plane. Let $\rho = c(\theta, t)$ be the image of the precursor shock in the ζ-plane. A normalized computational grid is then obtained by letting:

$$X = (\rho - 1)/(c - 1)$$

$$\theta = (\frac{\pi}{2} - \theta_o)\frac{\tanh[\alpha(Y-1)]}{\tanh \alpha} + \frac{\pi}{2} \qquad (48)$$

$$T = t$$

where θ_o is the constant value of θ which defines the rigid wall and which, in the present case, should be equal to zero. The computation is performed in the (X, Y) plane, using a rectangular grid with evenly spaced lines; it must be noted, however, that *X=constant lines and Y=constant lines on the physical plane are generally not orthogonal to each other*, since the boundary $\rho = c(\theta, t)$ is not constant with respect to θ. The lack of orthogonality, however, does not affect the accuracy of the results.

Since here two boundaries are defined by constant values of θ and of the other two boundaries one is defined by a constant value of ρ but the other by a value of ρ which depends on θ and t, it will be necessary to define X not only as a function of ρ but of θ and t; therefore, we will write:

$$X = X(\rho, \theta, t)$$

$$Y = Y(\theta) \qquad (49)$$

$$T = t$$

Letting

$$a_{11} = X_t + GuX_\rho + GvX_\theta/\rho \ , \quad a_{12} = \gamma G X_\rho \ , \quad b_{11} = GvY_\theta/\rho$$

- 15 -

$$b_{12} = \gamma G Y_\theta / \rho \ , \quad g_{12} = \gamma G X_\theta / \rho \ , \quad a_{21} = G \theta X_\rho \tag{50}$$

$$h_3 = G \theta X_\theta / \rho \ , \quad b_{21} = G \theta Y_\theta / \rho$$

and

$$F = [(\gamma-1)\Phi + \frac{\gamma}{P_r}\nabla^2\theta]/(pR_e) \tag{51}$$

$$c_1 = \gamma E - F$$

$$c_2 = vD - \frac{\theta G}{pR_e}[\frac{4}{3}\Delta_\rho - \Omega_\theta/\rho - j\frac{\ell}{Gy}\Omega]$$

$$\tag{52}$$

$$c_3 = -uD - \frac{\theta G}{pR_e}[\frac{4}{3}\Delta_\theta/\rho + \Omega_\rho + j\frac{\mathcal{S}}{Gy}\Omega]$$

the equations of motion are recast in the form:

$$P_T + a_{11}P_X + b_{11}P_Y + a_{12}u_X + b_{12}v_Y + g_{12}v_X + c_1 = 0$$

$$u_T + a_{11}u_X + b_{11}u_Y + a_{21}P_X + c_2 = 0$$

$$\tag{53}$$

$$v_T + a_{11}v_X + b_{11}v_Y + b_{21}P_Y + h_3 P_X + c_3 = 0$$

$$S_T + a_{11}S_X + b_{11}S_Y = F$$

It is easy to see that the first three equations (53) and the first three equations (65) have the same form as Equations (23) of [3]. The integration procedure explained in [3] can be applied. We expect the integration technique to provide a very good estimate of convection and wave-propagation effects which are common to inviscid and viscous flows.

- 16 -

8. Rigid boundaries

For a viscous flow, the velocity at a rigid boundary is assumed to vanish. There are no difficulties, thus, in the determination of u and v. Pressure and entropy require more care. We consider here the case of an isothermal wall; the temperature, θ is a prescribed constant. Because of (17), P and S are linearly related; therefore,

$$\frac{DS}{DT} = (1-\gamma)\, \frac{DP}{DT}$$

and consequently, the first of (46) must be replaced by

$$P_t + G(uP_\rho + \frac{v}{\rho} P_\theta) + G(u_\rho + \frac{1}{\rho} v_\theta) = 0 \tag{54}$$

having taken into account that E vanishes identically. The equations to be solved are still (53), provided that a_{12}, b_{12}, g_{11} and g_{12} are divided by γ and c_1 is set equal to zero.

Once the pressure has been determined, S is obtained from (17). Therefore, S is not calculated directly as a result of dissipation and heat transfer in the flow, because the condition of constant wall temperature implies some external action, and (17) gives us the final outcome of such action and the local variation of pressure.

9. Integration procedure

The equations of motion (53) are integrated following the general guidelines of Section 6 in [3]. We define

$$c_1^X = g_{11}u_Y + c_1 \quad , \quad c_2^X = b_{11}u_Y + h_2 P_Y + c_2$$

$$C_1^Y = g_{12} v_X \qquad , \qquad C_2^Y = a_{11} v_X + h_3 P_X + c_3 \tag{55}$$

After finding the characteristic slopes, λ_i^X, λ_i^Y (i=1,2) from

$$\begin{vmatrix} a_{11} - \lambda_i^X & a_{21} \\ \\ a_{12} & a_{11} - \lambda_i^X \end{vmatrix} = 0 \quad , \quad \begin{vmatrix} b_{11} - \lambda_i^Y & b_{21} \\ \\ b_{12} & b_{11} - \lambda_i^Y \end{vmatrix} = 0 \tag{56}$$

and letting

$$A_i = \frac{a_{11} - \lambda_i^X}{\lambda_2^X - \lambda_1^X} \quad , \quad B_i = \frac{b_{11} - \lambda_i^Y}{\lambda_2^Y - \lambda_1^Y}$$

$$\tag{57}$$

$$D_{ij}^X = \frac{a_{ij}}{\lambda_2^X - \lambda_1^X} \quad , \quad D_{ij}^Y = \frac{b_{ij}}{\lambda_2^Y - \lambda_1^Y}$$

the equations to be integrated are:

$$P_T^X + A_1 \lambda_1^X P_{X1} - A_2 \lambda_2^X P_{X2} + D_{12}^X (\lambda_2^X u_{X2} - \lambda_1^X u_{X1}) + C_1^X = 0$$

$$u_T + D_{21}^X (\lambda_2^X P_{X2} - \lambda_1^X P_{X1}) + A_1 \lambda_2^X u_{X2} - A_2 \lambda_1^X u_{X1} + C_2^X = 0 \tag{58}$$

and

$$P_T^Y + B_1 \lambda_1^Y P_{Y1} - B_2 \lambda_2^Y P_{Y2} + D_{12}^Y (\lambda_2^Y v_{Y2} - \lambda_1^Y v_{Y1}) + C_1^Y = 0$$

$$v_T + D_{21}^Y (\lambda_2^Y P_{Y2} - \lambda_1^Y P_{Y1}) + B_1 \lambda_2^Y v_{Y2} - B_2 \lambda_1^Y v_{Y1} + C_2^Y = 0 \tag{59}$$

with

$$P_T = P_T^X + P_T^Y \tag{60}$$

For discretization, the space derivatives are classified into three categories: (i) the ones explicitly appearing in (58) and (59), (ii) the ones explicitly appearing in (55), and (iii) the ones appearing in (51) and (52). The derivatives of the first category are discretized according to the rules (14) and

(15) of [3]; the derivatives of the second category according to the rules (34) and (35) of [3]; an the derivatives of the third category are approximated by ordinary centered differences, because the physical nature of the terms which they affect is diffusion. Few exceptions to the general rules are necessary for points on rigid boundaries or next to rigid boundaries. For points on rigid boundaries, the alternate two-point-three-point approximation is always taken using points inside the flow field. For points next to rigid boundaries, if use of a point located behind the wall were required in a three-point approximation, the latter is substituted by a two-point formula.

10. Numerical treatment of shocks

Shocks are generally present in a compressible flow field, either as boundaries or imbedded in the flow. In both cases, they can be treated numerically in the general framework of the computational technique described in the previous Sections. We begin with some general considerations.

Let $\vec{N}$ and $\vec{t}$ be the unit vector normal and tangential to a shock at any of its points, Q, respectively:

$$\vec{N} = N_1 \hat{\imath} + N_2 \hat{\jmath} \quad , \qquad \vec{t} = -N_2 \hat{\imath} + N_1 \hat{\jmath} \tag{61}$$

$\vec{W}$ the shock velocity,

$$\vec{W} = W \vec{N} \tag{62}$$

and $\tilde{u}$, $\tilde{v}$ the velocity components along $\vec{N}$ and $\vec{t}$, respectively:

$$
\begin{aligned}
\tilde{u} &= uN_1 + vN_2 & u &= \tilde{u}N_1 - \tilde{v}N_2 \\
\tilde{v} &= -uN_2 + vN_1 & v &= \tilde{u}N_2 + \tilde{v}N_1
\end{aligned}
\tag{63}
$$

The N-component of the velocity relative to the shock is

$$\tilde{u}_{rel} = \tilde{u} - W \qquad (64)$$

The relative normal Mach number on the low pressure side of the shock is

$$M^2_{n\,1rel} = \frac{\tilde{u}^2_{1rel}}{\gamma\theta_1} \qquad (65)$$

The Rankine-Hugoniot conditions are:

$$P_2 = P_1 + \ln\frac{2\gamma M^2_{n\,1rel}-\gamma+1}{\gamma+1} \qquad (66)$$

$$\tilde{u}_{2rel} = \frac{\gamma-1}{\gamma+1}\,\tilde{u}_{1rel} + \frac{2}{\gamma+1}\,\frac{\gamma\theta_1}{u_{1rel}}$$

We will need the derivatives of P_2 and u_{2rel} with respect to W:

$$\frac{\partial P_2}{\partial W} = -\frac{4\tilde{u}_{1rel}}{2\tilde{u}^2_{1rel}-(\gamma-1)\theta_1} \qquad (67)$$

$$\frac{\partial \tilde{u}_{2rel}}{\partial W} = -\frac{\gamma-1}{\gamma+1} + \frac{2}{\gamma+1}\,\frac{\gamma\theta_1}{\tilde{u}^2_{1rel}}$$

Let us assume that the shock is oriented in the general direction of the X=constant lines; therefore, it can be defined by its intersections, X_s, with Y=constant lines. At each intersection, we consider two points, one on the low-pressure side and the other on the high-pressure side. The point on the low-pressure side must be updated by using information proceeding from that side only. The point on the high-pressure side must be updated by using information from both sides. The information proceeding from the low-pressure side must satisfy the Rankine-Hugoniot conditions; the information proceeding from the high-pressure side is carried to the shock along a characteristic. The acceleration of the shock results from the compatibility of

the different information. To obtain the characteristic equation, we should rewrite the equations of motion in a frame relative to the moving shock, where the Y-coordinate of the shock is unchanged but its X-coordinate follows the shock in its motion. Therefore, we will introduce a new set of coordinates,

$$x = X - X_s(Y,T)$$

$$\epsilon = Y \tag{68}$$

$$\tau = T$$

and rewrite (65) in the form:

$$P_\tau + \alpha_{11}P_x + b_{11}P_\epsilon + \alpha_{12}u_x + b_{12}v_\epsilon + \gamma_{12}v_x + c_1 = 0$$

$$u_\tau + \alpha_{11}u_x + b_{11}u_\epsilon + \alpha_{21}P_x + h_2 P_\epsilon + c_2 = 0 \tag{69}$$

$$v_\tau + \alpha_{11}v_x + b_{11}v_\epsilon + b_{21}P_\epsilon + n_3 P_x + c_3 = 0$$

$$S_\tau + \alpha_{11}S_x + b_{11}S_\epsilon = F$$

where

$$\alpha_{11} = a_{11} - b_{11}X_{sY} - X_{sT} \ , \quad \alpha_{12} = a_{12} - g_{11}X_{sY} \ , \quad \alpha_{21} = a_{21} - h_2 X_{sY}$$

$$\gamma_{12} = g_{12} - b_{12}X_{sY} \ , \quad n_3 = h_3 - b_{21}X_{sY} \tag{70}$$

A characteristic equation may now be obtained, using x and τ as basic independent variables:

$$(\alpha_{11} - \lambda)(P_\tau + \lambda P_x) - \alpha_{12}(u_\tau + \lambda u_x) - \gamma_{12}(v_\tau + \lambda v_x) + R = 0 \tag{71}$$

where λ is the solution of the equation

$$\begin{vmatrix} \alpha_{11} - \lambda & \alpha_{21} & n_3 \\ \alpha_{12} & \alpha_{11} - \lambda & 0 \\ \gamma_{12} & 0 & \alpha_{11} - \lambda \end{vmatrix} = 0 \tag{72}$$

that is,

$$\lambda = \alpha_{11} \pm (\alpha_{12}\alpha_{21} + \gamma_{12}\eta_3)^{1/2} \tag{73}$$

and R comprises all the remaining terms.

Note now that

$$\alpha_{12} = \gamma G \nu N_1 \ , \quad \gamma_{12} = \gamma G \nu N_2$$

$$\alpha_{21} = G \theta \nu N_1 \ , \quad \eta_3 = G \theta \nu N_2 \tag{74}$$

where

$$\nu = \frac{(\alpha_{12}^2 + \gamma_{12}^2)^{1/2}}{\gamma G} \tag{75}$$

Therefore,

$$\alpha_{12} u + \gamma_{12} v = \gamma G \nu \tilde{u}$$

$$\alpha_{12} u_\tau + \gamma_{12} v_\tau = \gamma G \nu \tilde{u}_\tau - \gamma G \nu (u N_{1\tau} + v N_{2\tau}) \tag{76}$$

$$\alpha_{12} u_X + \gamma_{12} v_X = \gamma G \nu \tilde{u}_X$$

Instead of (71) we can write:

$$(\alpha_{11} - \lambda)(P_\tau + \lambda P_X) - \gamma G \nu (\tilde{u}_\tau + \lambda \tilde{u}_X) + R_1 = 0 \tag{77}$$

where

$$R_1 = R + \gamma G \nu (u N_{1\tau} - v N_{2\tau})$$

A further simplification is obtained by observing that

$$-\frac{\alpha_{11} - \lambda}{\gamma G \nu} = \pm \frac{(\alpha_{12}\alpha_{21} + \gamma_{12}\eta_3)^{1/2}}{\gamma G \nu} = \pm \frac{a}{\gamma} \tag{78}$$

because of (74) and (75), so that (77) can be written in the form:

$$\pm\frac{a}{\gamma} (P_\tau + \lambda P_\chi) + \tilde{u}_\tau + \lambda \tilde{u}_\chi + R_1 = 0 \qquad (79)$$

The values of P_τ and $\tilde{u}_\tau$, obtained by integrating the Navier-Stokes equations (69) using information from the high-pressure side of the shock only, must satisfy (79). On the other hand, the exact solution of the flow problem in the presence of the shock, which accounts also for the information from the low-pressure side and the Rankine-Hugoniot conditions, must satisfy (79) as well. Therefore, if we write (79) twice, once for the τ-derivatives as obtained from the Navier-Stokes equations (that is, using for the shock point the same integration procedure which is applied to other points) and again for the exact τ-derivatives and we subtract one equation from the other, the simple result is obtained:

$$\pm\frac{a}{\gamma}(P_\tau - P_\tau^{(NS)}) + \tilde{u}_\tau - \tilde{u}_\tau^{(NS)} = 0 \qquad (80)$$

where the derivatives obtained from the Navier-Stokes equations are labeled (NS) and the exact derivatives are unlabeled.

The latter derivatives can obviously be expressed in the form:

$$P_\tau = P_\tau^* + \frac{\partial P_2}{\partial W} W_\tau \quad , \quad \tilde{u}_\tau = \tilde{u}_\tau^* + \frac{\partial \tilde{u}_2}{\partial W} W_\tau \qquad (81)$$

where f_τ^* is a derivative computed considering W as a constant. The acceleration of the shock is thus obtained:

$$W_\tau = \frac{\pm a(P_\tau^{(NS)} - P_\tau^*) + \gamma(\tilde{u}_\tau^{(NS)} - \tilde{u}_\tau^*)}{\pm a \, \partial P_2/\partial W + \gamma \, \partial u_2/\partial W} \qquad (82)$$

Since both the starred derivatives and the derivatives indicated by (NS) are computed using the same initial values, (82) can be replaced by

$$W_\tau \Delta t = \frac{\pm a(P^{(NS)} - P^*) + \gamma(\tilde{u}^{(NS)} - \tilde{u}^*)}{\pm a \, \partial P_2/\partial W + \gamma \, \partial u_2/\partial W} \qquad (83)$$

- 23 -

where P^* and $\tilde{u}^*$ are the values on the high-pressure side of the shock obtained from updated values on the low-pressure side by applying the Rankine-Hugoniot conditions to a shock whose geometry has been updated but whose velocities, W, are still the same as at the beginning of the integration step. This result [4] is remarkable since it provides an extremely simple method for calculating the shock acceleration although it relies on the same basic concepts which have been shown to be necessary for a proper, physically correct, handling of shocks [5].

We will now consider first the case where the shock is a boundary, moving into a gas at rest, and then the case of an imbedded shock.

In the case of a shock moving into a gas at rest, let us assume that the shock is a right boundary of the computational field. It is, thus, defined by $X=1$; in this case, X, ϵ and τ coincide with X, Y and T, respectively and $\alpha_{11}=a_{11}$, $\alpha_{21}=a_{21}$, $\alpha_{12}=a_{12}$, $\gamma_{12}=g_{12}$, $\eta_3=h_3$. The characteristic reaching the shock from the high-pressure side is a right-running characteristic, and in the preceding equations, whereas a $\pm$ appears, the upper sign must be used. Note in addition that $\tilde{u}_1=0$ and $\tilde{v}_1=0$; therefore, $\tilde{u}_{1rel}=-W$ and $M^2_{n1rel}=W^2/\gamma$. In this case, obviously, the low-pressure side values are known without any need for computing; the (NS)-values on the high-pressure side are obtained together with and using the same procedure as for interior grid points.

For an imbedded shock, whose location does not generally coincide with a grid line, we use a simplified procedure to obtain the values at the shock on the low-pressure side and the (NS) values on the high-pressure side. On the low-pressure side, instead of integrating (69) (which would require a special, and not easy, redefinition of approximations for the x- and ϵ-derivatives), we simply assume that the values at the shock can be extrapolated from the two adjacent grid points on the same y=constant line, both at the end of the predictor and the corrector level. On the high-pressure side, we assume that the T-derivatives on the shock are equal to the T-derivatives at the grid point next to the shock on the same Y=constant line. Note, however, that

$$f_\tau = f_T + f_X \ X_{sT} \tag{84}$$

for any function f. The values of f_T at the shock are assumed to be the same as at the next grid point on the high-pressure side, on the same Y=constant line. The values of f_X are approximated as follows:

$$f_X = [f_A - f_s + \frac{1-\epsilon}{1+\epsilon} \ (f_B - f_s)]/\Delta X \tag{85}$$

where $\epsilon = (X_A - X_s)/\Delta X$ and A is the grid point next to the shock on the high-pressure side and B is the next grid point. This formula provides a smooth transition when the shock crosses an X=constant line.

For an imbedded shock, thus, the calculation proceeds as follows: In the predictor stage, after updating all grid points, the low-pressure side of the shock is obtained by extrapolation and (84) is also applied to P, u, v and S. The values on the high-pressure side are updated by adding $f_\tau \Delta t$ to the initial values of f; the values so obtained are the predicted $f^{(NS)}$. The predicted f* are obtained by applying (66) to the predicted values on the low-pressure side. Then, (83) is applied and W is temporarily updated, but its original value is retained in storage. The geometry of the shock is updated, considering that, in virtue of (62), (28) and (33),

$$\rho_{st} = G \ W/N_1 \tag{86}$$

and using the approximations:

$$\rho_s(t+\Delta t) = \rho_s(t) + \rho_{st}\Delta t + \frac{1}{2}\rho_{stt}\Delta t^2 \tag{87}$$

where the second derivatives are obtained by differentiating (86). In the corrector stage, the procedure outlined above for the predictor stage is repeated through the application of (84). The updating of the values on the high-pressure side is obtained by adding

$$\frac{1}{2} \ (f_\tau - f_\tau^{(pred)})\Delta t$$

to the predicted values. The corrected f* are obtained by apply-

ing (66) to the corrected values on the low-pressure side, with the original value of W. Then, (83) is applied again and W is definitively updated. The Rankine-Hugoniot conditions (66) are applied once more to the corrected values on the low-pressure side using the final value of W, to obtain the final values on the high-pressure side. The entropy is also computed from

$$S_2 = S_1 + P_2 - P_1 - \gamma \ln(\tilde{u}_{1rel}/\tilde{u}_{2rel}) \qquad (88)$$

At this stage, it is convenient to correct the values at the grid point next to the shock on the high-pressure side. Pressure and velocity components are interpolated from the values at the shock and the following grid point. Entropy is also interpolated considering that it is carried along a streamline.

11. Details of the calculation

The calculation is started at a small, positive value of t, when the precursor shock has already moved from the muzzle mouth. Initially, the shock is assumed to lie on a ρ=constant line (with the value of the constant, c_o, slightly greater than 1), and all parameters pertinent to the shock are assumed equal to their values at t=0. Note that, since the flow behind the shock is uniform, the shock Mach number defines pressure, velocity and entropy. Uniform flow is assumed between the muzzle mouth and the shock, if the gas is inviscid. The velocity component, v is made equal to zero throughout.

Initially, the computational region is divided only into two strips along the X-axis. Along the Y-axis we consider as many partitions as necessary to provide sufficient resolution.

Since the flow is viscous, we need some modifications to the initial conditions near the wall, to account for the vanishing of the velocity at the wall. The precursor shock cannot reach the wall; the perturbation front, elsewhere in the form of a shock, becomes a characteristic at the wall. Therefore, on the initial ρ=c line which represents the shock, P is assumed equal

- 26 -

to zero at the wall. On the next wall point, P is taken equal to one half of its value behind the shock. The wall temperature is assumed equal to 1 at any time. The entropy is defined accordingly. The u-velocity component is taken equal to one half of its value behind the shock along the second θ=constant line from the wall.

From the initial conditions, the calculation proceeds as detailed above. We note that the centerline is computed as a symmetry line, not as a rigid wall. For computational purposes, the shock geometry is prolonged to the wall with a constant value of c, and the wall point is computed as any other wall point, taking advantage of the fact that the state of the gas in front of the perturbed region is known. A similar procedure is automatically applied to any other point on the perturbation front, if the shock happens to lose its strength completely; that is, the point on the perturbation front is computed as any interior, shockless point, taking advantage of the fact that the state of the gas in front of the perturbed region is known.

As the calculation proceeds, the number of grid intervals in the X-direction is doubled every time (c-1) on the centerline exceeds 1.4 times its initial value or the value it had at the previous doubling, until the total number of intervals is 16.

Certain features of the flow are common to the inviscid and viscous models. An expansion appears from the beginning near the inlet of the duct; the region of maximum expansion moves from left to right, but at a slower speed than the precursor shock. Consequently, even with the precursor shock losing strength, the pressure behind it remains higher than the lowest pressure already attained along the duct. The particles are accelerated and then decelerated again. A compression wave appears, which tends to steepen up, as every compression wave does, and another shock results eventually.

In the presence of viscosity, the recompression wave and the secondary shock strongly interact with the boundary layer in the process of formation. The latter thickens and separates very soon. Between the main stream and the wall, a wide dead-water region appears, where the pressure tends to equalize the ambient

pressure (in front of the precursor shock). The separated flow never reattaches and becomes a plume. From the separation point on, the plume is insensitive to the wall geometry and the flow inside it is essentially inviscid. The results of the calculation of a steady, inviscid flow in a plume can be used to judge whether the viscous calculation approaches its theoretical asymptote, and how well.

Three cases have been calculated, with different values of θ_o and of the initial conditions. The first deals with a high value of θ_o, by virtue of which the flow occurs in a divergent (two-dimensional) channel. The second and the third use $\theta_o=0$. The second, however, does not contemplate initial conditions consistent with the flow in the barrel described in Section 3; rather, it has initial conditions consistent with a shock-tube experiment [19]. The third case is consistent with the barrel flow described in Section 3.

12. First example

In the first example, θ_o has been taken equal to 1.2. and r_o equal to 2.2603. Therefore, the calculation attempts to describe the flow in a diverging channel, inserted at the end of a straight shock tube (Fig. 4). The flow is assumed to be two-dimensional. The stretching parameter, α, has been taken equal to 2, and the sector between $\theta=\theta_o$ and $\theta=\pi/2$ is divided into 16 intervals. Consequently, we obtain a fair accumulation of grid lines near the wall, and still work with a reasonably small number of lines. It is clear, however, that the resolution is well below the limits which are usually recommended for a good description of Reynolds number effects; the lack of an adequate resolution is particularly felt in the vicinity of the plume shear layer. Nevertheless, the present results are very encouraging, just because very good qualitative results are obtained with such a coarse mesh. The Reynolds number used in this case is extremely high (10^6), so that the flow should be considered as inviscid practically everywhere, except across the boundary layer. We know, however, as we said in the preceding

First example
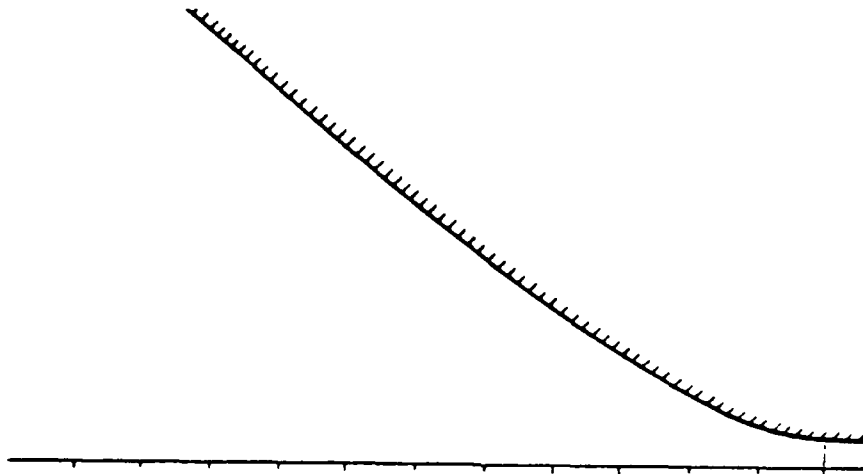
Fig. 4

section, that the steady configuration of the flow in a channel whose area increases beyond any limit is a plume, that is, a separated flow. The plume exists, regardless of the value of the Reynolds number; only the thickness of the shear layer limiting the plume reveals what the Reynolds number is. In the present case, we should expect the formation of a plume with a limiting shear layer of practically vanishingly small thickness; but we also know that such a picture is going to be distorted by the artificial Reynolds number of the computational mesh, which is smaller by orders of magnitude.

The Prandtl number is taken equal to 1, and γ equal to 1.4. The temperature at the wall is assumed to be equal to 1, that is, to the temperature of the gas at rest. The value of P at the inlet is 1.6487. Consistent values of u and S are u=1.6551, S=0.1702. The Mach number at the inlet is barely supersonic, M=1.040.

The progression of the precursor shock and the flow evolution behind it are shown in Fig. 5 by sets of isobars drawn at different instants of time. The figures represent the lower half of the channel. On the symmetry line, notches denote intervals of unit length. The isobars correspond to constant values of P, spaced as indicated by the value of DREF in each picture; the

First example

RUN 33, K,T= 400   0.6665, LINE= 1   OREF,LAST REF= 0.040 1.640
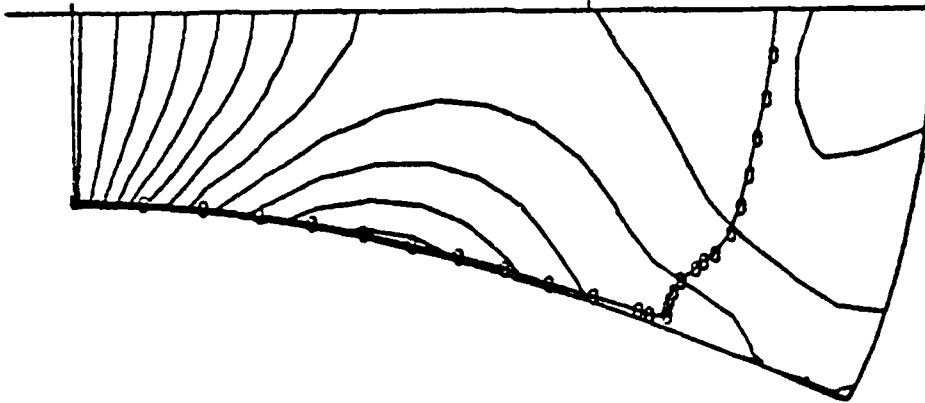
RUN 33, K,T= 800   1.3718, LINE= 1   OREF,LAST REF= 0.050 1.600
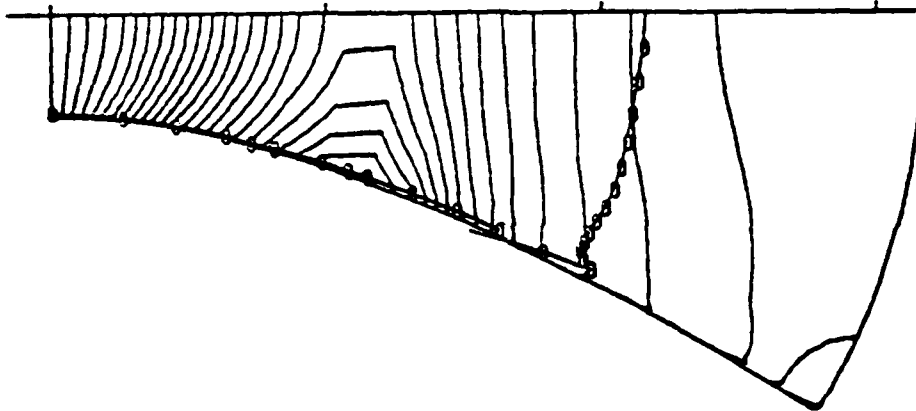
RUN 33, K,T= 1200   2.1100, LINE= 1   OREF,LAST REF= 0.100 1.600
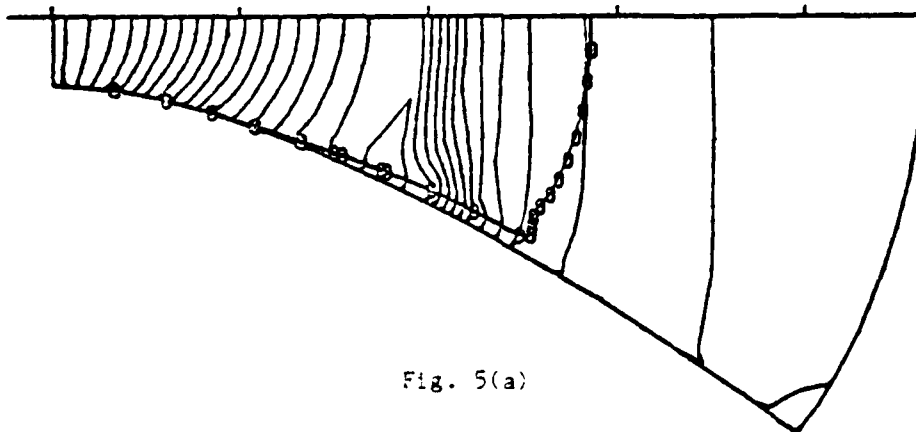
Fig. 5(a)

First example

RUN 35, K,T= 1900   3.4774, LINE= 1   DREF,LAST REF= 0.200 1.600
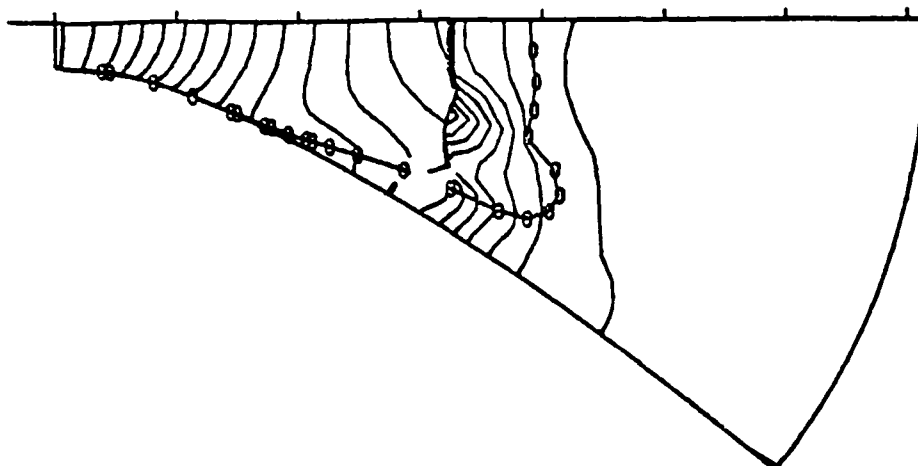
RUN 35, K,T= 2400   4.5097, LINE= 1   DREF,LAST REF= 0.200 1.600
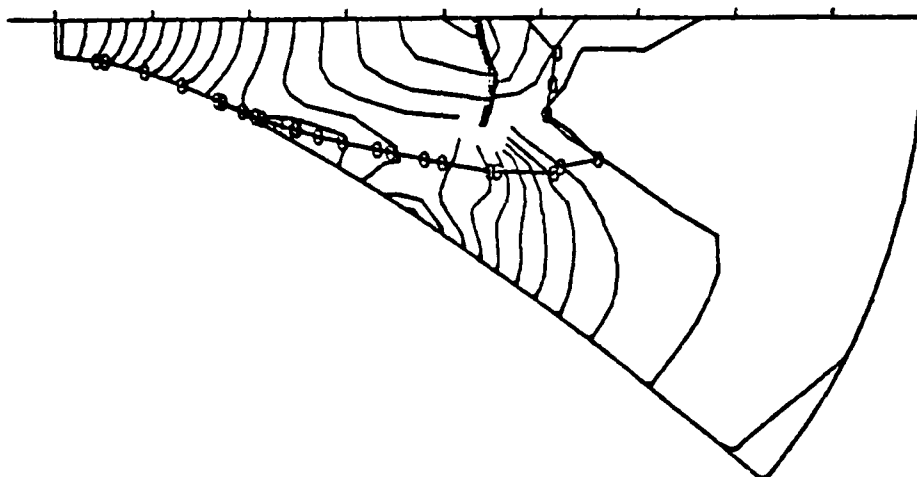
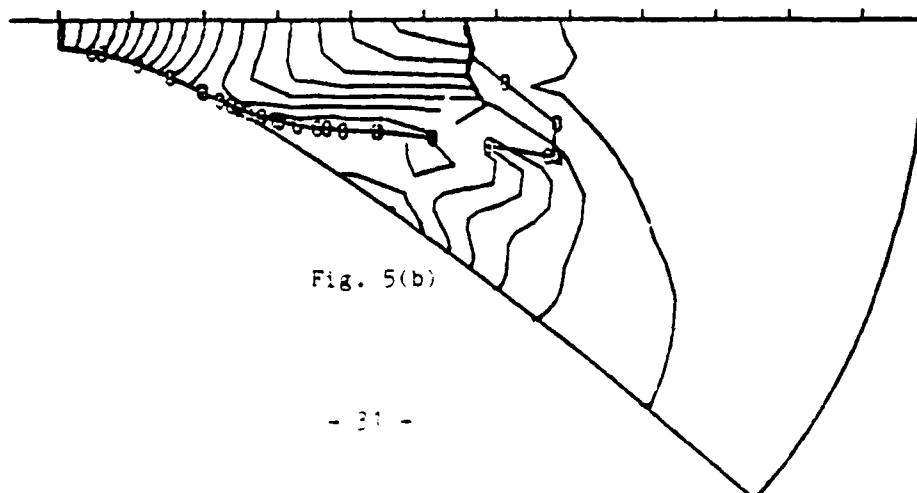RUN 35, K,T= 3200   6.2530, LINE= 1   DREF,LAST REF= 0.200 1.600

Fig. 5(b)

- 31 -

lines marked with 0 are sonic lines.

At t=0.6665, the expansion has barely begun and is still very mild; at t=1.3718 it is stronger (the lowest value of P is less than 0.5) and the recompression is clearly taking shape. Within the first unit length of the channel, the interaction of up- and down-running characteristics is very clear (an obvious consequence of M being very close to 1 at the start); the recompression, therefore, appears almost as unidimensional. At t=2.1100, the recompression is clearly piling up at two unit lengths from the entrance; the lowest value of P is below the ambient value. As indicated by the modified shape of the sonic line, a small separated region appears; this effect is much clearer in Fig. 6, where pictures of streamlines are shown. A shock is soon formed, and it is evident in the isobar plot at t=3.4774 (the thickness of different arcs of the shock is proportional to its local strength). The second drawing in Fig. 6 clearly shows the separation of the flow at t=4.0914. The streamlines in the separated region should not be interpreted as picturing a flow as strong as the main flow; as a matter of fact, the velocities in the separated region are extremely small, in general.

The isobar picture at t=4.5097 shows a changing pattern; the recompression shock shrinks towards the symmetry line, and all isobars with negative values of P (that is, below ambient pressure), as well as the P=0 line, show a definite tendency to bend horizontally in the direction of the flow. At t=6.2530, the qualitative description of the plume is correct, but resolution has become so poor that most of the quantitative results are distorted.

Nevertheless, it may be interesting to see how close the flow is to a steady, inviscid plume, at this early stage of evolution. To this effect, a program was written to describe a steady, two-dimensional, shockless inviscid plume evolving from the same inlet conditions along the same channel geometry until the ambient pressure is reached, and then continuing inside the region delimited by a p=constant streamline. The corresponding isobar pattern, with values of P spaced 0.25 apart, is shown in the upper part of Fig. 7. Isobars from the last plot of Fig. 5,

First example

RUN 35. K.T= 1200   2.1100, LINE= 7
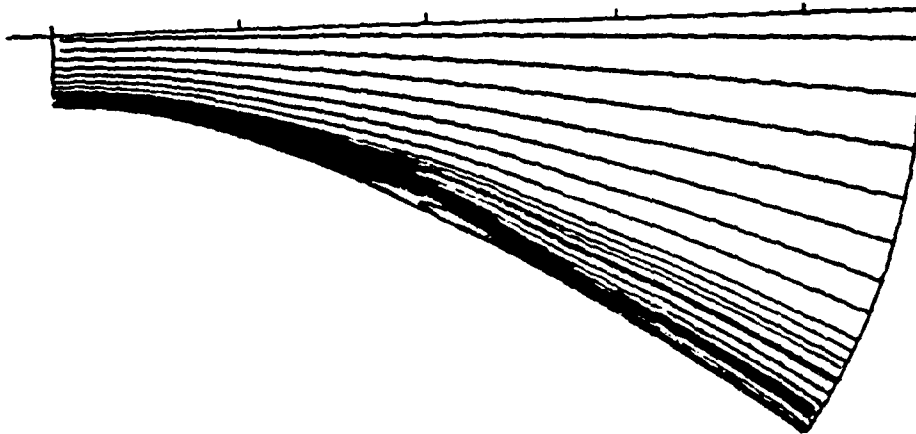
KUN 35, K.T= 2200   4.8914, LINE= 7

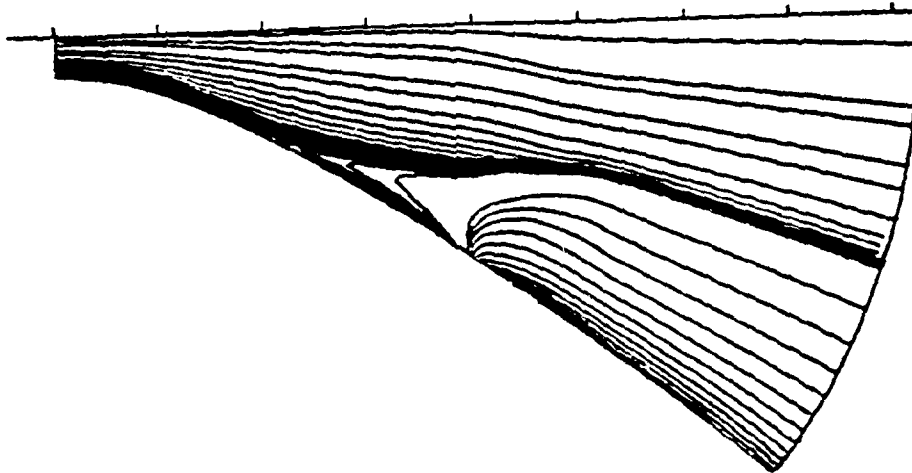Fig. 6(a)
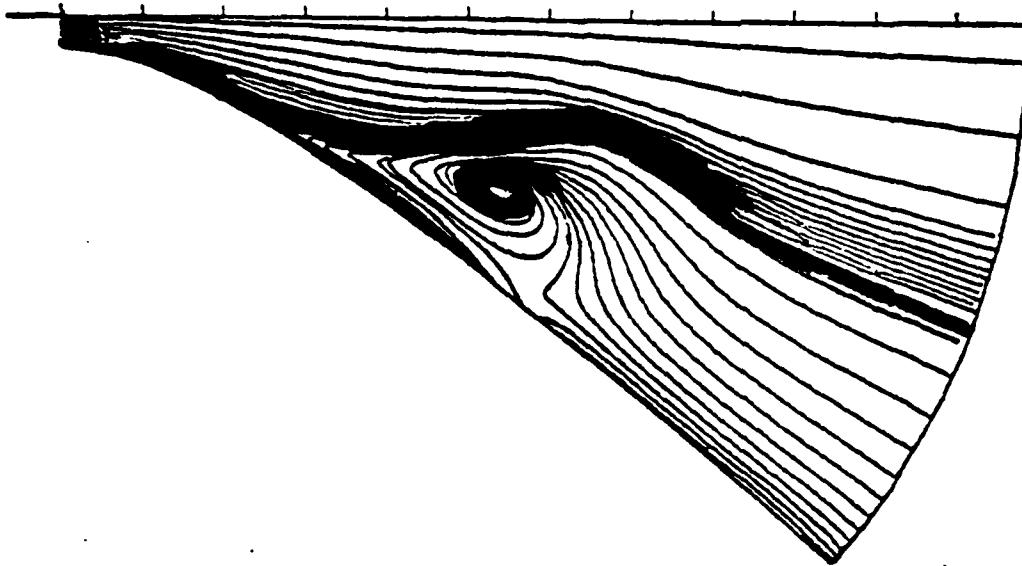
First example

FUN 35. K.T= 3208   6.2538, LINE= 7

Fig. 6(b)

interpolated at the same values of P, are shown in the lower part
of Fig. 7. At this stage, with no supporting calculations on a
finer grid, it is not possible to state whether the overexpansion
shown by the latter is a temporary effect, tending to disappear
in a further stage of evolution, or simply the result of lack of
resolution (note that the steady plume calculation has 20 inter-
vals along any line orthogonal to the symmetry line and hundreds
of steps along the channel, whereas the lower figure has been
computed on the grid of Fig. 4).

13. Second example

A second example was run, based on experiments performed
on a muzzle jet flow simulator [19]. The experimental device
consists of a shock tube, opening into a low-pressure chamber.
The flow is axisymmetrical. The outer radius of the shock tube

- 34 -

Second example
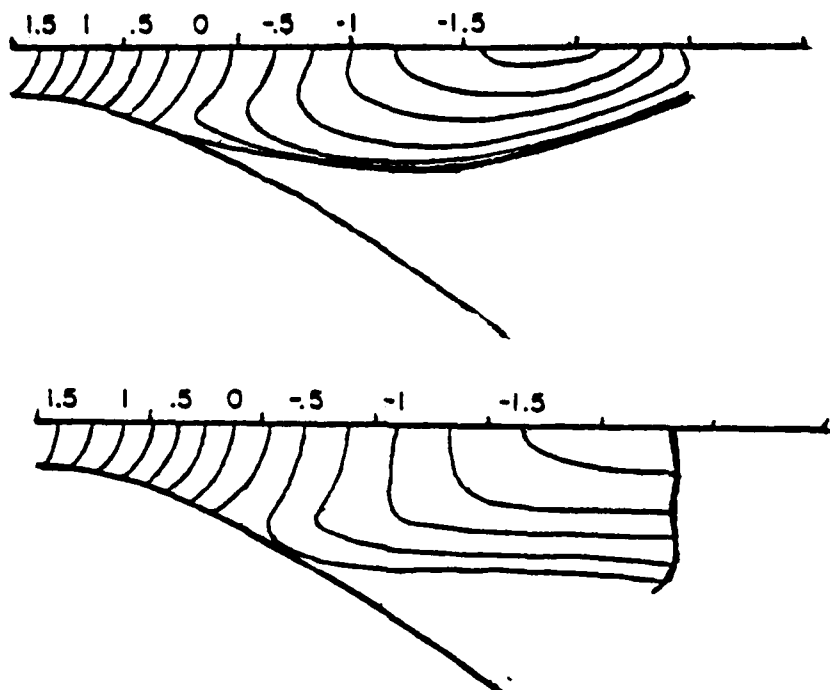
Fig. 7

is 2.08 times the inner radius. The latter is 19 mm. At sea level, the speed of sound is 360 m/sec; therefore our reference velocity is 304.25 m/sec. Assuming that the kinematic viscosity of air is 1.6×10^{-3} m^2/sec, the Reynolds number is approximately 3600. We take the Prandtl number equal to 1 and $\gamma = 1.4$. We will try to simulate the experiment shown in Fig. 7 of [19]; therefore, we will use a value of P at the shock tube mouth equal to 3.40. Consistent values of u and S are u=4.8250, S=1.1387. The Mach number is 1.6680.

The evolution of the flow is shown in Fig. 8 by sets of isobars drawn at different instants of time, as it was made in Fig. 5. Our results can be compared to Fig. 7 of [19], taking into account that our reference time is 0.0624 msec.

In Fig. 9, the location of the precursor shock and of the recompression shock on the centerline is plotted as a function of time; experimental results from Fig. 14 of [19] are also plotted in the same figure.

Third example

RUN 41, K,T= 200   0.0786, LINE= 1   RUN 41, K,T= 400   0.1583, LINE= 1

DREF,LAST REF= 0.200 3.400   DREF,LAST REF= 0.200 3.600
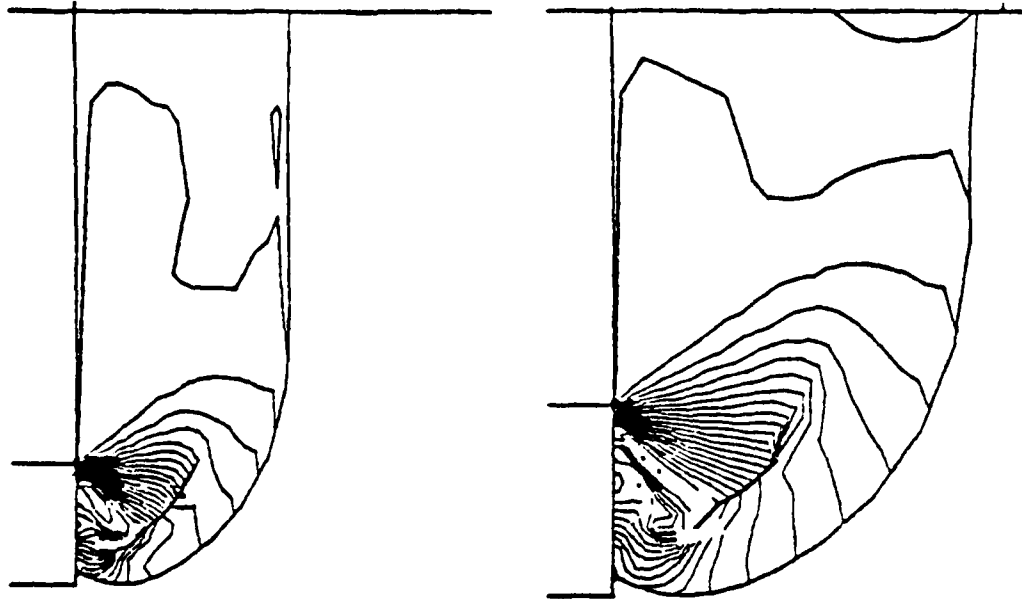
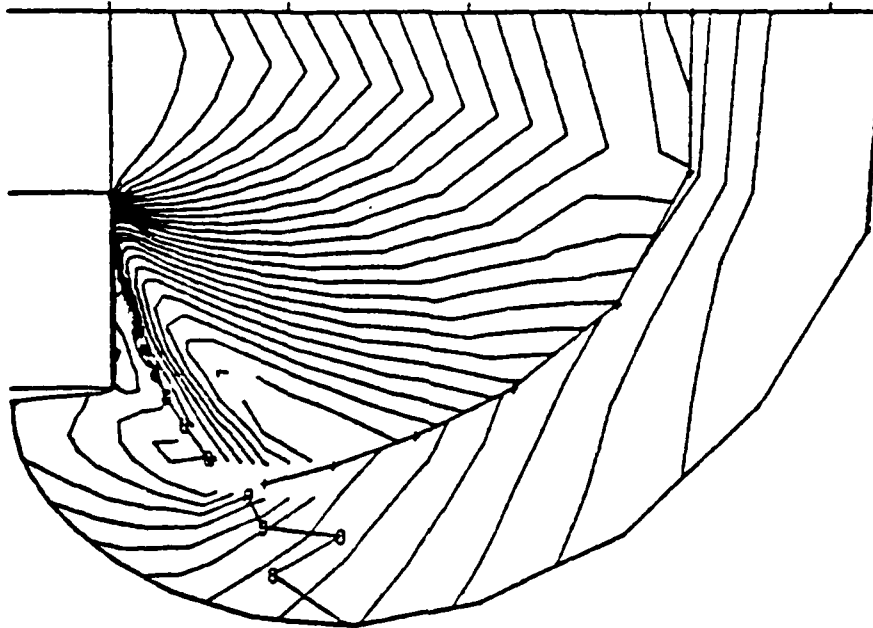RUN 23, K,T= 900   0.4995, LINE= 1   DREF,LAST REF= 0.200 3.200
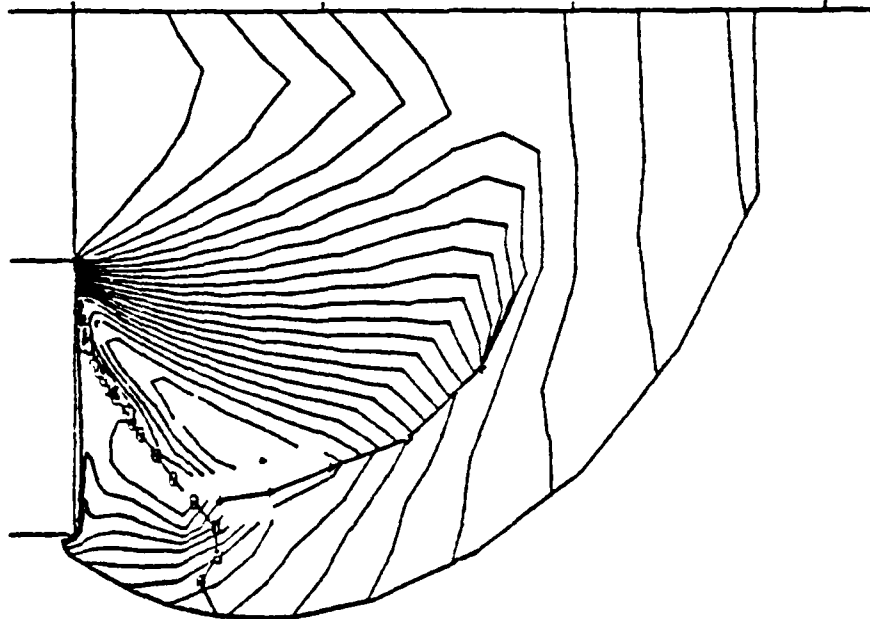
Fig. 8(a)

Third example

RUN 24. K.T= 1208   0.8818. LINE= 1   OREF.LAST REF= 0.200 3.200

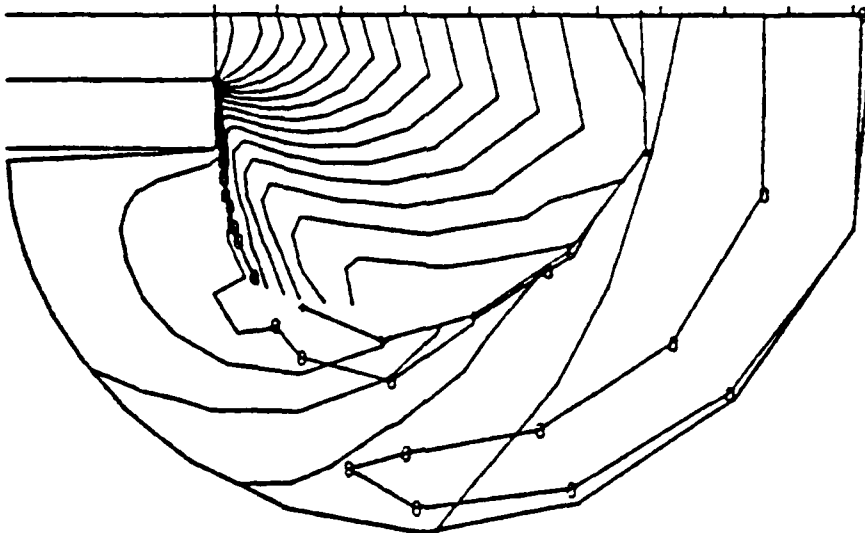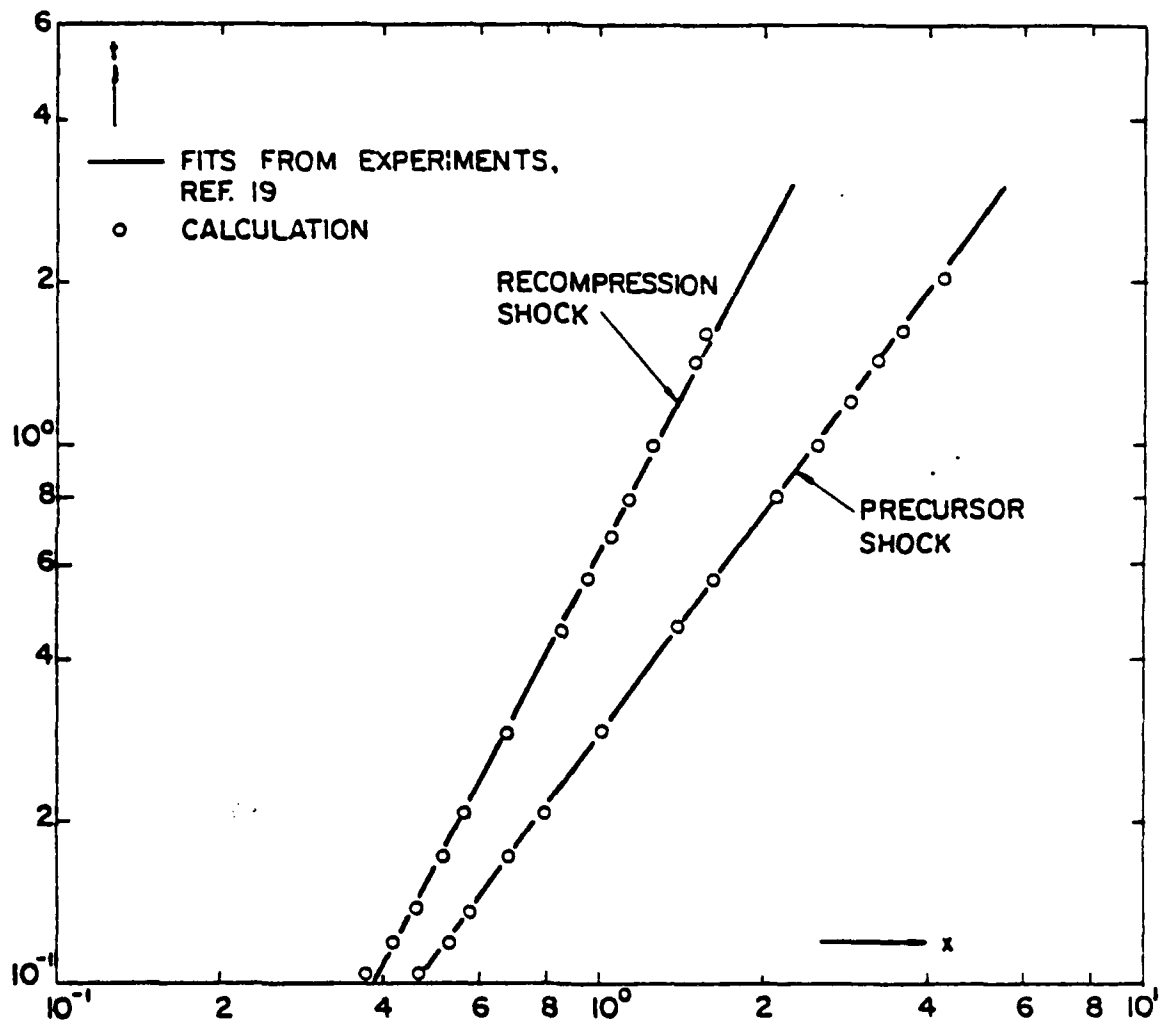RUN 24. K.T= 2350   3.0103. LINE= 1   OREF.LAST REF= 0.400 3.200


Fig. 8(b)

Fig. 9

14. Third example

Finally, a calculation was made to simulate experiments by Schmidt and Shear on the M-16 rifle [20]. Assuming the inner radius of the gun as the unit length, the outer radius is 2.2603 and the distance to be traversed by the nose of the bullet before it reaches the muzzle is 150.82. We are now using a program which couples the inner and outer flow calculations, and we determine the inner flow as in the first example. The conditions outside the gun at the instant of firing are assumed as the standard sea level conditions. The pressure ratio immediately after the precursor shock at the instant of its exit is 11.61 (slightly less than the one mentioned in [20]; the difference is due to the fact that the flow velocity behind the shock when it reaches the mouth of the barrel is lower than the bullet velocity when the base of the bullet separates from the muzzle). To compare calculations and experiments, we note first that our reference time [equal to the reference length, 2.7813 mm, multiplied by the square root of γ and divided by the speed of sound of the gas at rest (360 m/sec)], is 9.1 μsec. The precursor shock exits from the barrel at t=108, that is, .983 msec after firing. To reach that stage, about 700 computational steps were necessary, in which the one-dimensional internal flow alone was computed.

A set of isobar plots, at different instants of time, is presented in Fig. 10. The structure of the precursor blast compares well with the experimental evidence. The plot at t=110.1263 and the one at t=113.3647 are very close to the pictures shown as a) and b) in Fig. 3 of [20], which correspond to the same instants of time. A striking agreement is shown by the locations of blast shock and recompression shock on the centerline (Fig. 12). The straight lines in the figure are the ones defined in [20] as the best fit for their experimental values. Note that the instant at which the base of the bullet separates from the muzzle is, in our non-dimensional time, practically equal to 10. The position of the recompression shock is shown, at successive instants of time, in Fig. 12. Here we may note an

Third example

RUN 1, K.T= 1000 109.1071. LINE= 1
DREF.LAST REF= 0.200 2.400
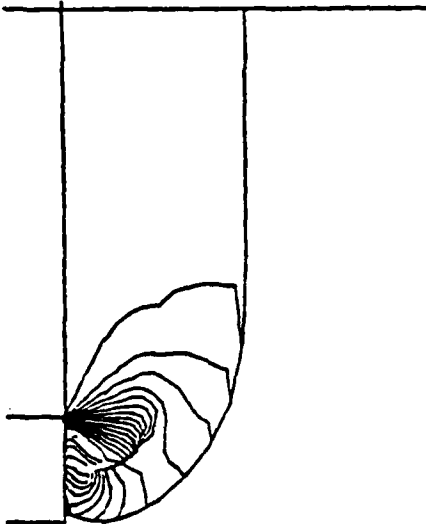
RUN 1, K.T= 1700 103 3347. LINE= 1
DREF.LAST REF= 0.200 2.600
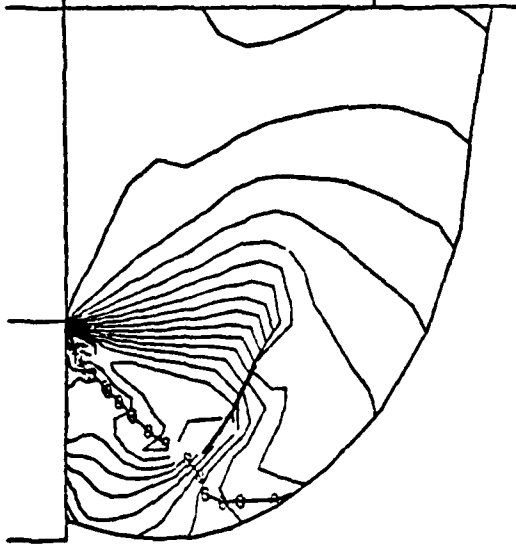
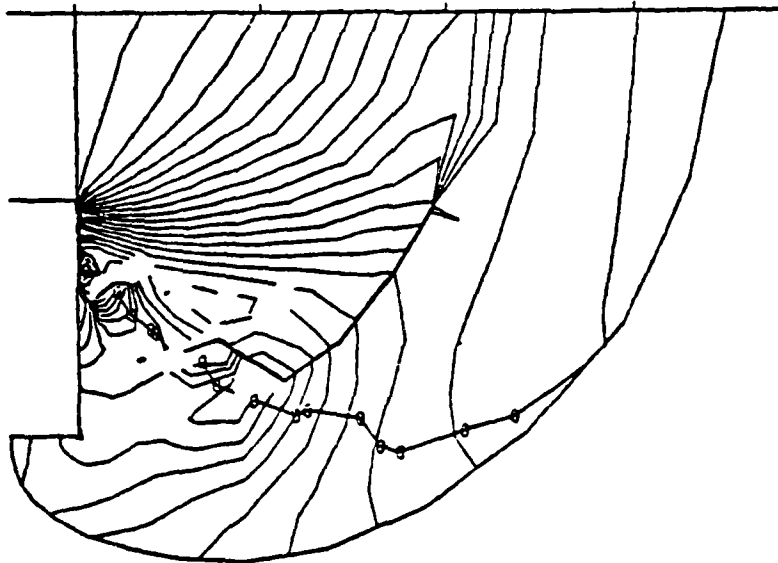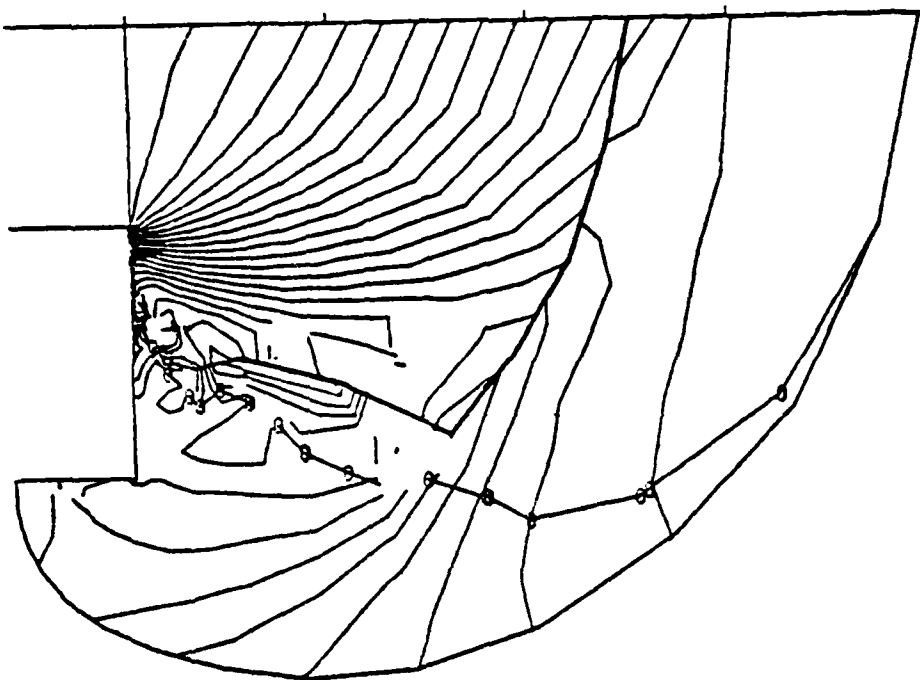RUN 1, K.T= 2200 109 8002. LINE= 1   DREF.LAST REF= 0.200 2.400

Fig. 10(a)

Third example

RUN 1. K.T= 3300 109.1911, LINE= 1 OREF,LAST REF= 0.200 2.400

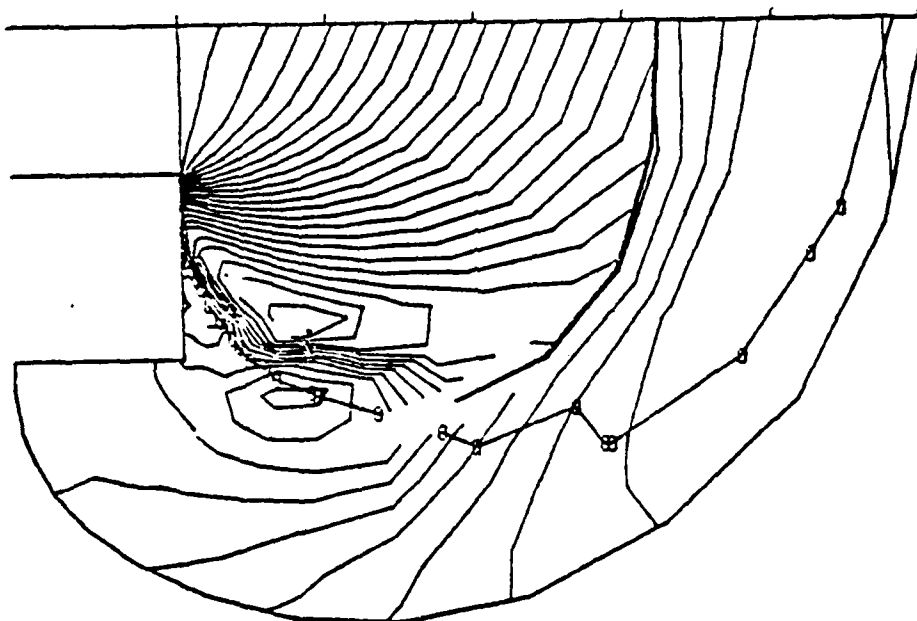RUN 2, K.T= 2500 109.6441. LINE= 1 OREF,LAST REF= 0.200 2.400
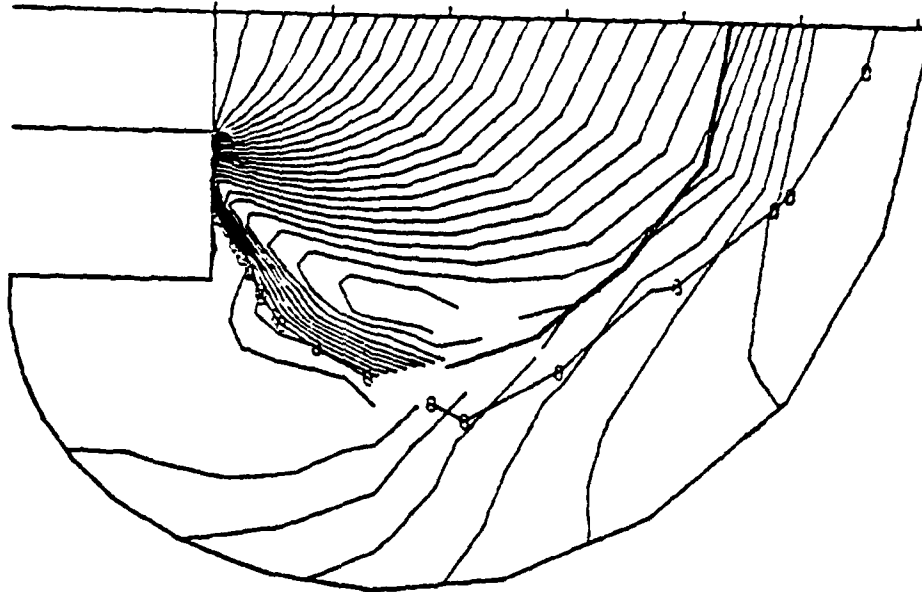
Fig. 10(b)

Third example

RUN   2. K.T= 2700   110 1353. LINE= 1   OREF.LAST REF= 0.200   2.400

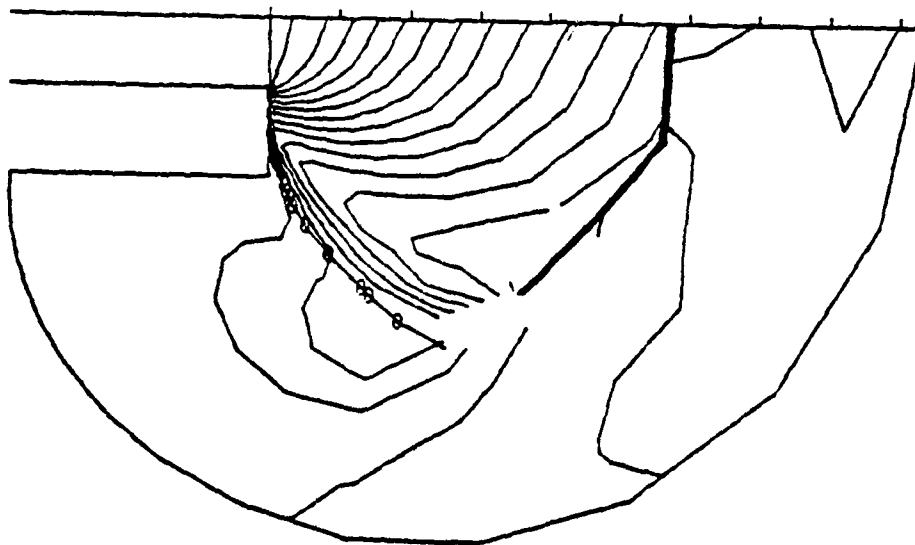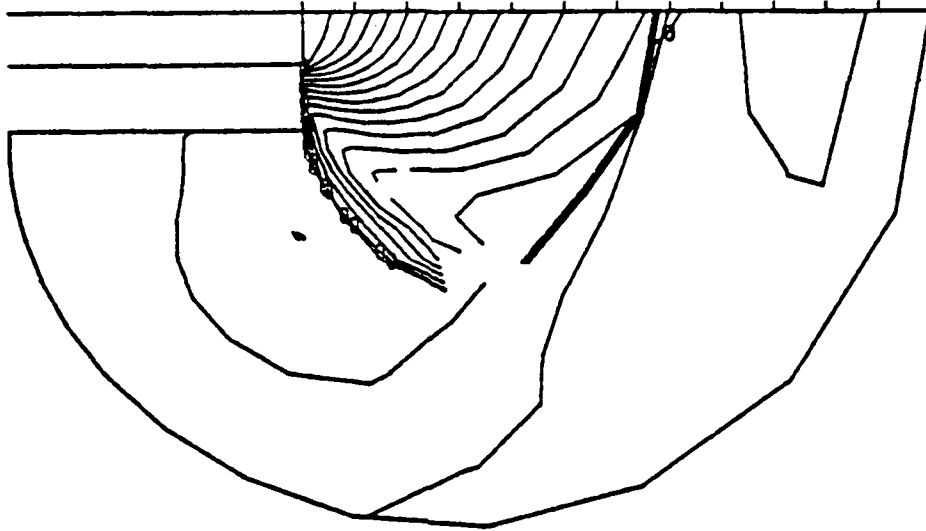RUN   2. K.T= 3300   111 7714. LINE= 1   OREF.LAST REF= 0.400   2.400

Fig. 10(c)

Third example

RUN   2, K.T= 3900 113.3647, LINE= 1   OREF,LAST REF= 0.400 2.400

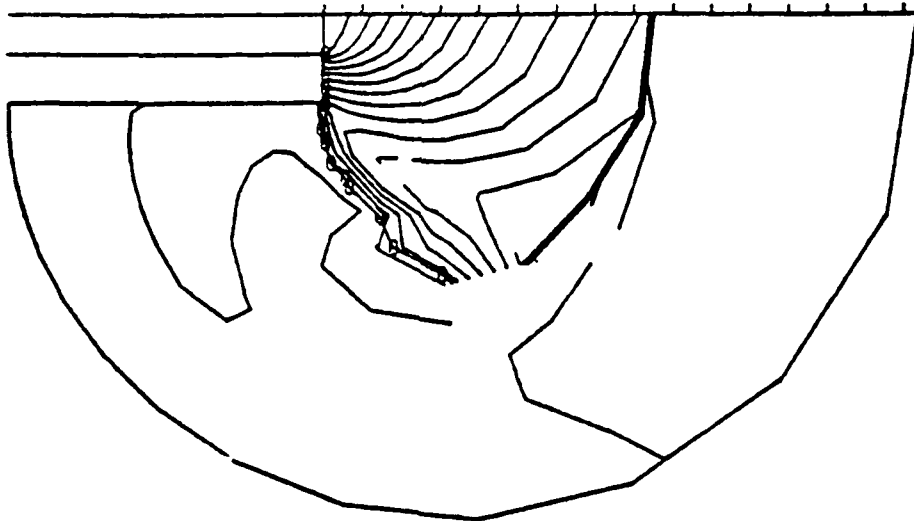RUN   2, K.T= 4414 115.5254, LINE= 1   OREF,LAST REF= 0.500 2.500

Fig. 10(d)

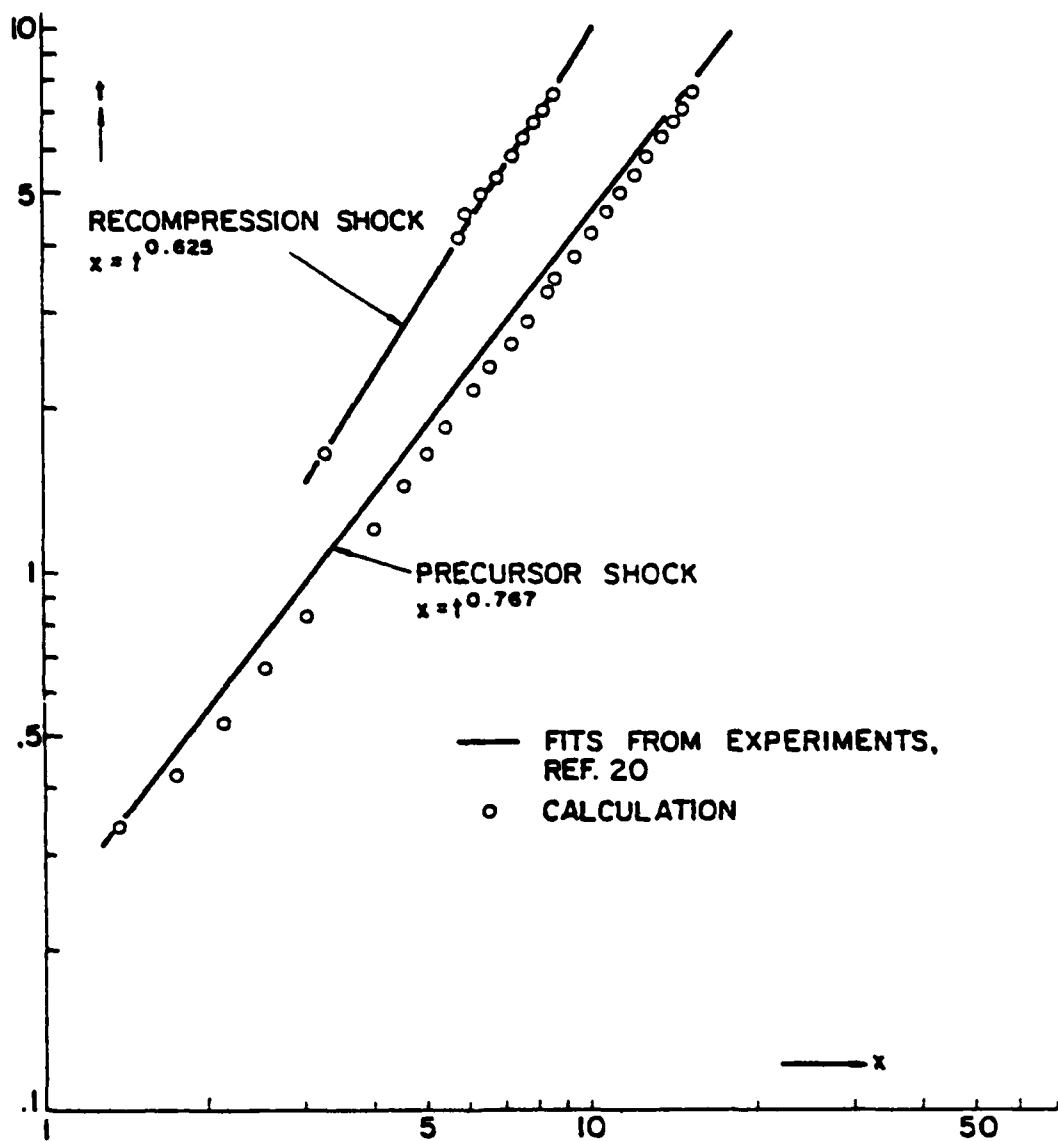Fig. 11

interesting numerical effect, which confirms our belief that shocks should be fitted. In the initial phase of evolution the shock, as computed, clearly shows two parts, one of which is what [20] calls a Mach disc and the other is the beginning of a plume shock; both are in the right position, according to the experimental evidence. Unfortunately, the way the imbedded shock is computed does not allow a single shock with a sharp corner to subsist indefinitely; the corner itself is dragged backwards by the 'plume' branch which, in turn, develops oscillations, sending numerical errors to other regions of the flow. Since a perfect determination of the plume shock was not considered of primary importance in this phase of the research, that branch was artificially deleted and not allowed to form again. In other words, our current results reflect an attempt to 'capture' the plume shock; the effect is clearly shown in Fig. 12; the edge of the plume is pushed outwards and the Mach disc (which itself, for being fitted, is properly located) is much wider than in the exper-
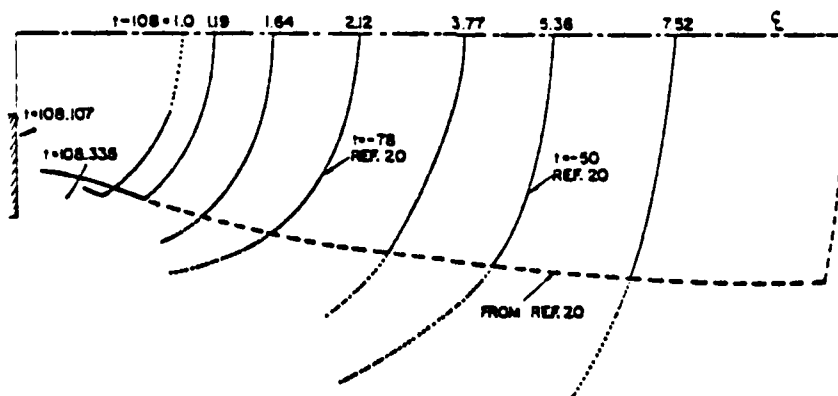
Fig. 12

iments.

To complete the description of the flow, we present a streamline picture, a plot of constant Mach lines, a plot of isentropics and a plot of velocity vectors in Figs. 13 and 14. All these figures refer to the instant of emersion of the bullet.

15. Second phase of precursor shock evolution

The last output of the run presented in the preceding section shows the perturbed flow field around the muzzle as the bullet is about to emerge from the barrel. To continue the analysis until the bullet is totally emerged, the computational program must be modified. Although only few statements have to be added or changed in the program used for the preceding analysis in order to produce the program used for the current one, the underlying algebraic manipulations are much more complicated because the $X=0$ line is now the image of the bullet's moving wall (in full or partially); consequently, a time–dependent mapping function is to be used.

In lieu of (22), we use the mapping sequence:

$$z = (r_0/\pi)[(z_1^2 - 1/z_1^2)/2 - \log z_1^2 - i\pi]$$

$$z_1 + 1/z_1 = 2B(\zeta_2 + 1/\zeta_2)$$

$$(\zeta_2 - 1)/(\zeta_2 + 1) = [(\zeta_1 - 1)/(\zeta_1 + 1)]^\delta$$

$$\zeta_1 = (\zeta - d^2/\zeta)/(1 - d^2)$$

(89)

where δ and d are functions of time. This means that the time associated with the coordinates, x and y, of the physical plane, cannot be confused with the time associated with the coordinates, ρ and θ, of the mapped plane. We will, thus, denote the first by t and the second by τ. The value of d is determined to assure correspondence between $\zeta = i$ and $z = \beta$, where β is the abscissa of the nose of the bullet. The value of δ is made equal to $1/2$

Second phase of precursor shock evolution

RUN 40, K.T= 2966   7.7684, LINE= 7
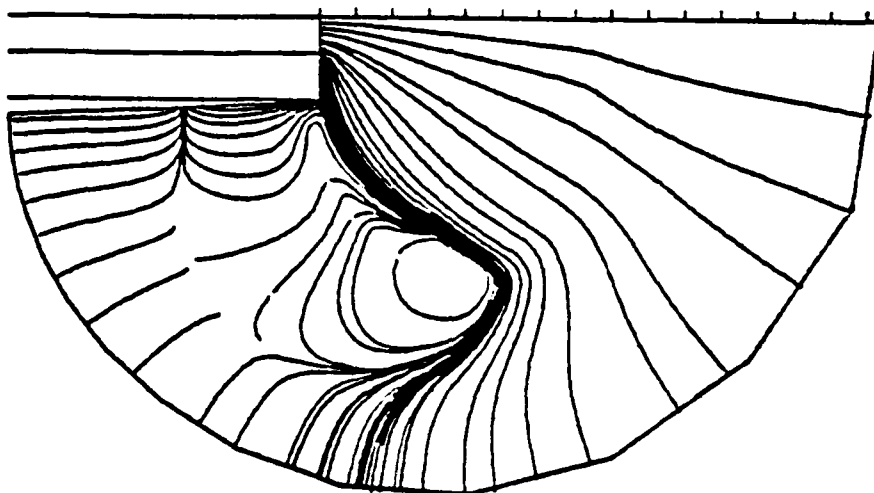
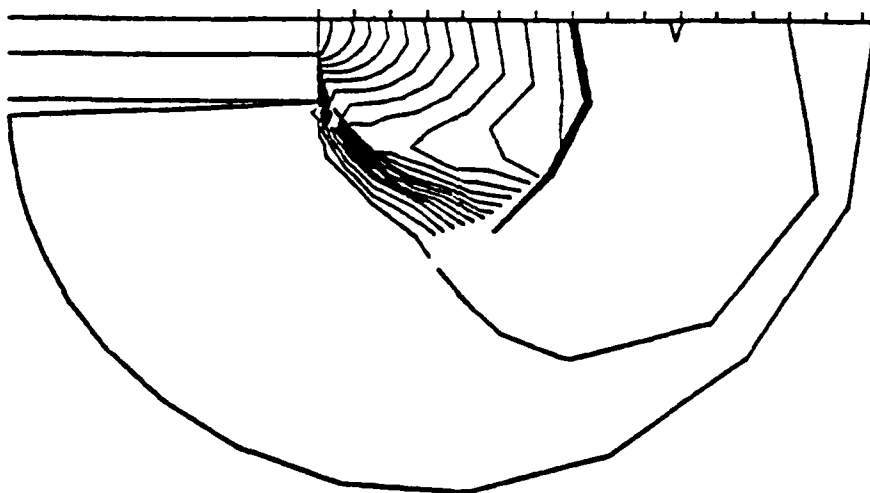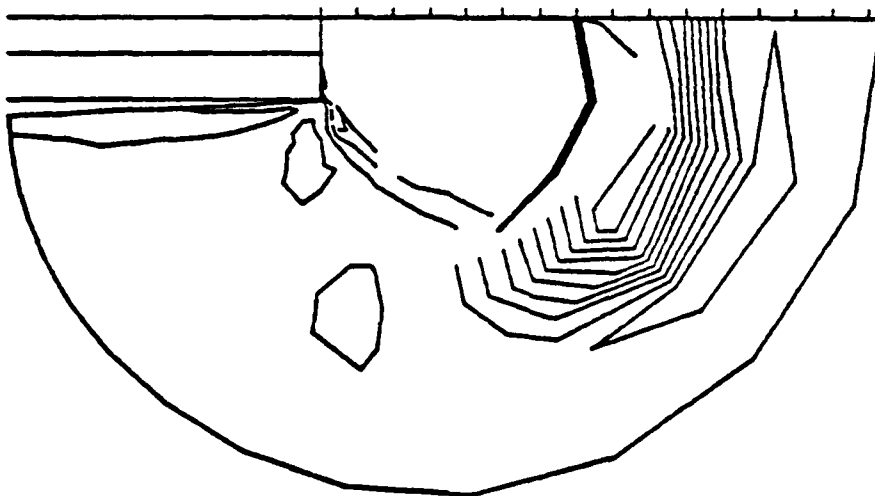RUN 40, K.T= 2966   7.7684, LINE= 2   OREF,LAST REF= 0.400 5.600

Fig. 13

Second phase of precursor shock evolution

RUN 40, K,T= 2966   7.7684, LINE= 4   OREF,LAST REF= 8.200 1.888
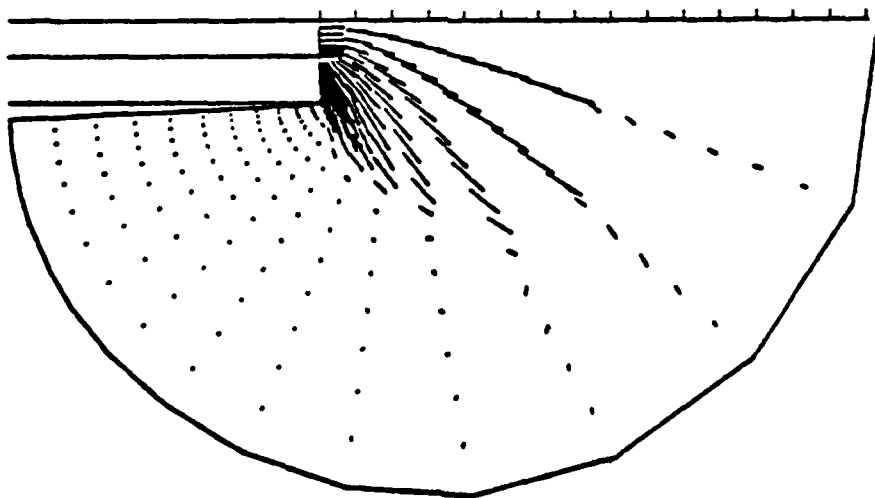
RUN 40, K,T= 2966   7.7684, LINE= 8

Fig. 14

when the cylindrical part of the bullet begins showing out of the barrel, and kept constant thereafter. During the emersion of the bullet nose, δ is varied between 0 and 1/2 using some arbitrary law, for example linearly.

The new mapping is provided to maintain the computational grid as close to orthogonal as possible, despite the appearance of a new boundary, and to keep the line X=0 as close as possible to a ρ=constant line. By no means, however, can such a simple mapping as (89) make the X=0 line to coincide exactly with a ρ=constant line. It is necessary, thus, to introduce the image of the boundary, opposite to the precursor shock, in the form $\rho = b(\theta,\tau)$, and to normalize the grid with the following transformation, which replaces (48):

$$X = (\rho - b)/(c - b)$$

$$\theta = (\frac{\pi}{2} - \theta_o)\frac{\tanh[\alpha(Y-1)]}{\tanh\alpha} + \frac{\pi}{2} \tag{90}$$

$$T = \tau$$

In addition to the definitions of z, ζ, g, ϕ, $\mathcal{L}$ and $\mathcal{S}$ given by (20), (21), (23), (26) and (24), we need to define the quantities:

$$f = \frac{\partial\log \zeta}{\partial t} = f_1 + i\, f_2 \tag{91}$$

$$\psi = \frac{\partial\log g}{\partial t} = \psi_1 + i\, \psi_2 \tag{92}$$

From (89) we obtain

$$f = \frac{1}{\zeta}\left\{\frac{2d}{1-d^2}(\zeta_1 - \frac{1}{\zeta})d_t - \frac{\zeta_1^2-1}{2\delta}\log\frac{\zeta_1-1}{\zeta_1+1}\delta_t\right\}\frac{d\zeta}{d\zeta_1} \tag{93}$$

$$\psi = -2dd_t[\frac{1}{1-d^2} + \frac{1}{\zeta^2+d^2}] + 2f\frac{d^2}{\zeta^2+d^2} - \frac{1}{\delta}[1 + \zeta_1\log\frac{\zeta_1-1}{\zeta_1+1}]\delta_t \tag{94}$$

The relations given by (28), (29), (30) and (31) must be complemented by the following expressions:

$$\rho_t = \rho f_1 \, , \quad \theta_t = f_2 \, , \quad \tau_x = 0 \, , \quad \tau_y = 0 \, , \quad \tau_t = 1 \qquad (95)$$

$$x_\tau = (\mathcal{S}f_2 - \mathcal{L}f_1)\rho/G \, , \quad y_\tau = -(\mathcal{S}f_1 + \mathcal{L}f_2)\rho/G$$

$$t_\rho = 0 \, , \quad t_\theta = 0 \, , \quad t_\tau = 1 \qquad (96)$$

$$G_\tau = g(\psi_1 - \phi_1 f_1 + \phi_2 f_2) \, , \quad \omega_\tau = \psi_2 - \phi_1 f_2 - \phi_2 f_1 \qquad (97)$$

Between ρ, θ, τ and X, Y, T, the following relations hold:

$$\rho_X = 1/X_\rho \, , \quad \rho_Y = - X_\theta/(X_\rho Y_\theta) \, , \quad \rho_T = - X_\tau/X_\rho$$

$$\theta_X = 0 \, , \quad \theta_Y = 1/Y_\theta \, , \quad \theta_T = 0 \qquad (98)$$

$$\tau_X = 0 \, , \quad \tau_Y = 0 \, , \quad \tau_T = 1$$

$$X_\rho = 1/\rho_X \, , \quad X_\theta = - \rho_Y/(\rho_X \theta_Y) \, , \quad X_\tau = - \rho_T/\rho_X$$

$$Y_\rho = 0 \, , \quad Y_\theta = 1/\theta_Y \, , \quad Y_\tau = 0 \qquad (99)$$

$$T_\rho = 0 \, , \quad T_\theta = 0 \, , \quad T_\tau = 1$$

Consequently,

$$x_X = \mathcal{L}/GX_\rho \, , \quad x_Y = -(\mathcal{L}X_\theta/\rho X_\rho + \mathcal{S})\rho/GY_\theta \, , \quad x_T = -\mathcal{L}X_\tau/GX_\rho - (\mathcal{L}f_1 - \mathcal{S}f_2)\rho/G$$

$$y_X = \mathcal{S}/GX_\rho \, , \quad y_Y = (\mathcal{L} - \mathcal{S}X_\theta/\rho X_\rho)\rho/GY_\theta \, , \quad y_T = -\mathcal{S}X_\tau/GX_\rho - (\mathcal{S}f_1 + \mathcal{L}f_2)\rho/G$$

$$t_X = 0 \, , \quad t_Y = 0 \, , \quad t_T = 1 \qquad (100)$$

and

$$G_x = (\mathcal{L}\phi_1 + \mathcal{S}\phi_2)G^2/\rho \, , \quad G_y = (\mathcal{S}\phi_1 - \mathcal{L}\phi_2)G^2/\rho \, , \quad G_t = G\psi_1$$

$$\omega_x = (\mathcal{L}\phi_2 - \mathcal{S}\phi_1)G/\rho \, , \quad \omega_y = (\mathcal{L}\phi_1 + \mathcal{S}\phi_2)G/\rho \, , \quad \omega_t = \psi_2 \qquad (101)$$

From (90), it follows that

$$X_\rho = 1/(c-b) \, , \quad X_\theta = X_\rho[(X-1)b_\theta - Xc_\theta] \, , \quad X_\tau = X_\rho[(X-1)b_\tau - Xc_\tau] \qquad (102)$$

$$\theta_Y = [D^2 - (\theta-\pi/2)^2]\alpha/D \qquad (103)$$

with

$$D = (\pi - \theta_0)/\tanh \alpha \qquad (104)$$

Certain second derivatives are also needed, to evaluate viscous terms:

$$X_{\rho\rho}=0, \quad X_{\rho\theta}\approx X_\rho^2(b_\theta - c_\theta)$$

$$X_{\theta\theta}\approx X_{\rho\theta}X_\theta/X_\rho + X_\rho[X_\theta(b_\theta-c_\theta)+(X-1)b_{\theta\theta}-Xc_{\theta\theta}] \qquad (105)$$

$$Y_{\rho\rho}=0 \ , \quad Y_{\rho\theta}=0 \ , \quad Y_{\theta\theta}=(2\alpha/D)\ Y_\theta^2\ (\theta-\pi/2)$$

Let Q be a point on the physical plane:

$$Q = x\hat{I} + y\hat{J} \qquad (106)$$

Because of (100), it turns out that

$$G\ Q_X = (1/X_\rho)\hat{I} \ , \quad GY_\theta Q_Y = -(X_\theta/X_\rho)\hat{I} + \rho\hat{J}$$

$$G\ Q_T = -(X_\tau/X_\rho+\rho f_1)\hat{I} - \rho f_2\hat{J} \qquad (107)$$

The normal, $\hat{N}$ to an X = constant line is defined by

$$\hat{N} \cdot Q_Y = 0 \qquad (108)$$

Therefore, its components in the $\hat{I}$-and $\hat{J}$-directions, respectively, are

$$N_1 = 1/\nu \ , \quad N_2 = (X_\theta/\rho X_\rho)N_1 \qquad (109)$$

with

$$\nu = [1+(X_\theta/\rho X_\rho)^2]^{1/2} \qquad (110)$$

At the body, $\rho = b$, $X_\theta/\rho X_\rho = -b_\theta/b$, $X_\tau/X_\rho = -b_\tau$, $b_\tau = b_T$ and

$$b_t = b_\tau + \rho_t + b_\theta \theta_t = b_\tau + \rho f_1 + b_\theta f_2 \qquad (111)$$

Let

$$F(x,y,t) = 0 \qquad (112)$$

be the equation of the $X = 0$ line in the physical plane. Then $F_Y = 0$, that is

$$F_x(\mathscr{L}b_\theta - \mathscr{S}b) + F_y(\mathscr{S}b_\theta + \mathscr{L}b) = 0 \qquad (113)$$

Therefore,

$$b_\theta/b = (\mathscr{S}F_x - \mathscr{L}F_y)/(\mathscr{L}F_x + \mathscr{S}F_y) \qquad (114)$$

Similarly, $F_T = 0$, that is

$$F_x[\mathscr{L}b_\tau - b(\mathscr{L}f_1 - \mathscr{S}f_2)] + F_y[\mathscr{S}b_\tau - b(\mathscr{S}f_1 + \mathscr{L}f_2)] + GF_t = 0 \qquad (115)$$

Therefore,

$$b_t = \frac{b[(\mathscr{L}f_1 - \mathscr{S}f_2)F_x + (\mathscr{S}f_1 + \mathscr{L}f_2)F_y] - GF_t}{\mathscr{L}F_x + \mathscr{S}F_y} \qquad (116)$$

In the present run, the bullet has been assumed as a cylinder, with an elliptic nose. Let x_o be the abscissa of the center of the ellipse, which travels along the centerline at a constant speed; let a be the major axis of the ellipse. Therefore, for the nose,

$$F = (x+x_o)^2 + a^2 y^2 - a^2 = 0 \qquad (117)$$

$$f_x = 2(x+x_o) , \quad f_y = 2a^2 y , \quad F_t = 2(x+x_o)x_{ot} \qquad (118)$$

In the cylindrical part,

$$F = y+1 \ , \quad F_x = 0 \ , \quad F_y = 1 \ , \quad F_t = 0 \tag{119}$$

The calculation is then carried on in a way similar to the one performed in the absence of the bullet. Obviously, the velocity of the flow on the wall of the bullet equals $x_o \hat{\mathbf{1}}$. In addition, as a first step towards the simulation of spillage between bullet and barrel, the pressure at the rim of the bore is allowed to increase linearly with time, beginning when the nose of the bullet is almost completely out.

A further remark is necessary for a proper evaluation of the shocks. The image of a shock in the mapped plane is

$$\zeta_s = \rho_s \, e^{i\theta} \tag{120}$$

In the (ρ, θ) plane, we see variations in the time τ:

$$(\zeta_s)_\tau = \frac{\cdot d\zeta_s}{dz} \frac{dz_s}{dt} + \zeta_s \frac{\partial \log \zeta_s}{\partial t} \tag{121}$$

The first term in the right hand side is produced by the variation of z_s in time, the second term by the changes in the mapping parameters (the derivative is made at a constant z_s). The shock point, however, is always taken on a $\theta =$ constant line. Therefore,

$$(\zeta_s)_\tau = (\rho_s)_\tau e^{i\theta} = (\rho_s)_\tau \zeta_s / \rho_s \tag{122}$$

that is,

$$(\rho_s)_\tau \zeta_s / \rho_s = g \, dz_s/dt + \zeta_s f \tag{123}$$

With Q defined by (106),

$$W = \frac{dQ}{dt} . \hat{\mathbf{N}} \tag{124}$$

(33) can be used to replace $\hat{\mathbf{1}}$ and $\hat{\mathbf{J}}$ and then (123) to replace x_{st} and y_{st}; after simplifying, one obtains

$$(\rho_s)_\tau = GW/N_1 + c \, (f_1 + f_2 N_2/N_1) \tag{125}$$

- 53 -

which replaces (86).

The sequence of isobar plots of Fig. 15 describes the computed flow field around a protruding bullet which has the speed and the size, if not exactly the shape, of the bullet in [20]. Contrary to all the preceding plots, the ones in Fig. 15 are confined to a relatively small region in the vicinity of the bullet, since the rest of the flow is uneventful. The mesh is indeed very coarse; nevertheless, a good amount of information is still obtainable.

It should be noted that the speed of the flow in front of the bullet is higher than the speed of the bullet itself; in fact, the flow is accelerated by the supersonic expansion occurring around the lip of the muzzle. Therefore, the advancing bullet acts on the surrounding flow as a receding wall acts on a gas at rest, and produces a further expansion.
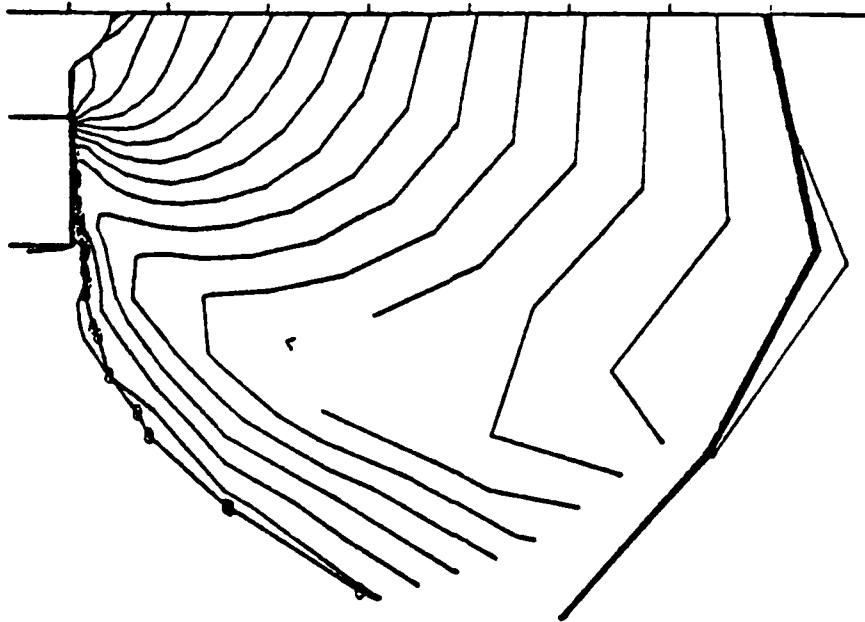
16. Conclusions and recommendations

The results of our numerical tests show that the basic features of our technique, viz. grid definition, integration scheme and shock fitting, do indeed provide very high accuracy. The minimal amount of grid points used also assures that the present calculations are much faster than any other, provided that the stepsizes are comparable. No total running time on a large-scale computer can be mentioned yet, since all calculations have been performed on a minicomputer (PDP 11/40) which not only is very slow, by current standards, but also has storage requirements that in turn force the program to be written in a highly inefficient way.

Before giving the analysis a full certificate of reliability, however, further research is needed. The shock-fitting section of the program must be recoded, in order to let the plume branch of the shock be tracked; this may imply a deep revision of some of the discretized equations used in the fitting because the plume shock stretches obliquely with respect to the computational

RUN 62, K,T= 50   0 1532, LINE= 1   DPEF,LAST REF= 0.400 2.400

RUN 62, K,T= 150   0.5926, LINE= 1   DREF,LAST REF= 0.400 2.400
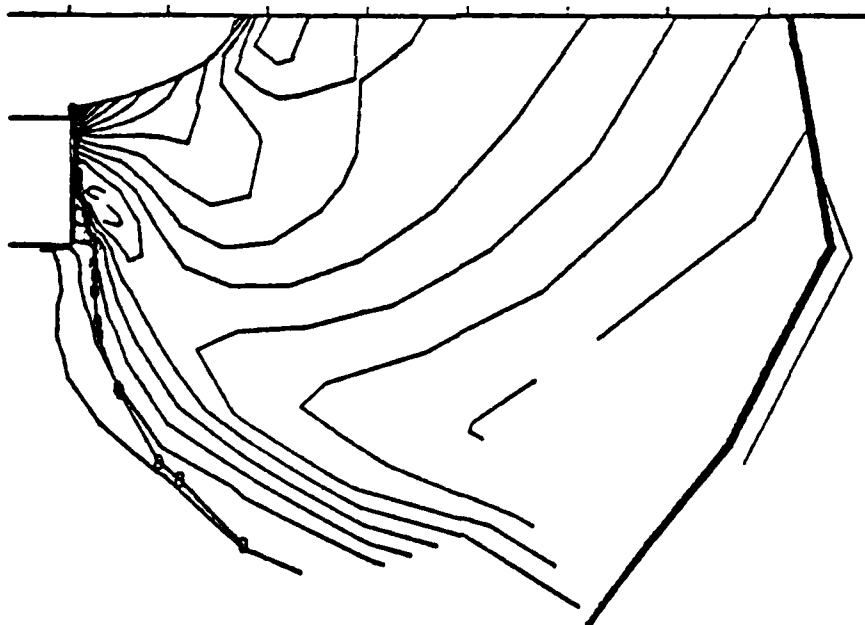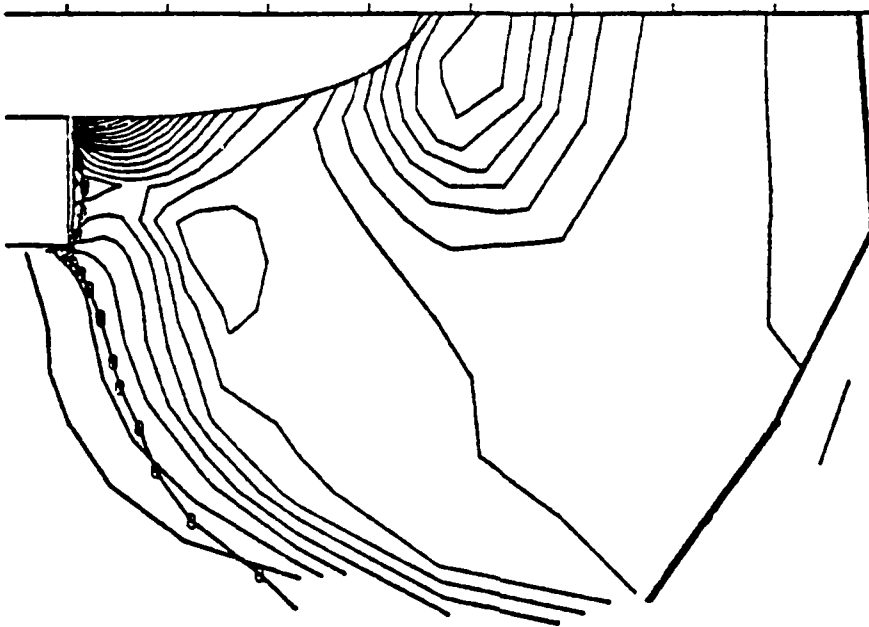
Fig. 15(a)

RUN 62. K.T= 300   1.2424, LINE= 1   OREF,LAST REF= 0.500 4.000

RUN 62. K.T= 400   1.9232, LINE= 1   OREF,LAST REF= 1.000 4.000
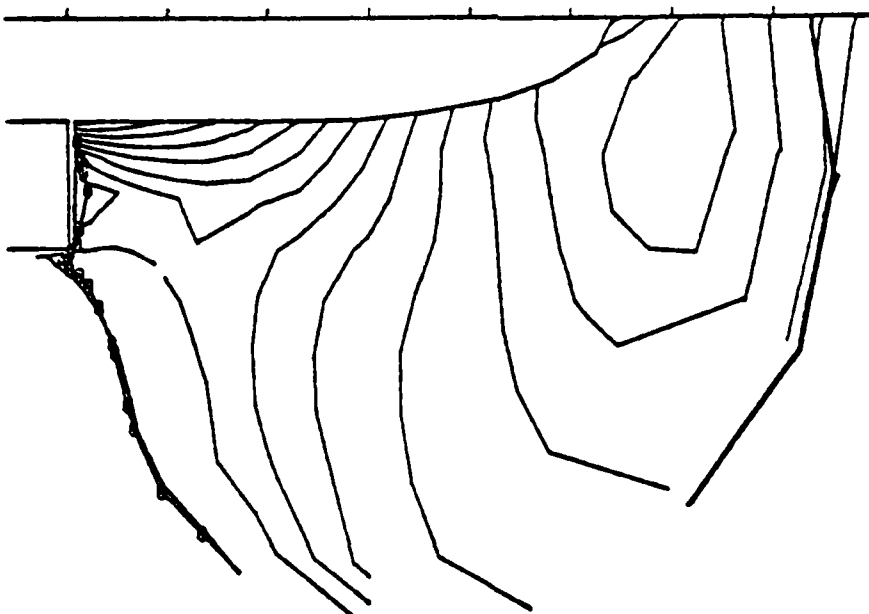
Fig. 15(b)

grid, whereas the recompression shock in the vicinity of the centerline tends to lie parallel to ρ=constant lines. In addition, some numerical difficulties may arise at the intersection of the two branches of the shock, which has the physical nature of a triple point.

The dependence of the results on the Reynolds number should also be investigated thoroughly. So far, we have concentrated grid lines near the rigid wall but we have made no attempt to compare our flows to boundary value results in that neighborhood. Moreover, the edge of the plume is a region of high viscous stresses, which our mesh is totally inadequate to calculate. Three different approaches should be considered, to improve the present results. The first consists of using a stretching in the θ-direction which concentrates grid lines where the vorticity is the highest. The second (and more difficult, but perhaps richer in consequences) consists of a fitting of the shear layer, the middle line of which should be tracked as a line floating within mesh points. The third approach would push this concept to its extreme consequences, totally eliminating the calculation of viscous terms and replacing shear layer by vortical discontinuities. An inviscid calculation, not requiring extremely fine grids and the processing of the viscous terms, would yield a very welcome reduction in running time.

If such a stage could be reached, we would consider it proper to compare results with those of a (not yet existing) purely inviscid code, where the mechanism for the onset of a plume configuration is provided by the appearance of a short shock, normal to the wall, totally independent on the recompression shock, as described in the present paper.

17. References

1. E.M. Schmidt, The effect of muzzle jet asymmetry on projectile motion, BRL Report R1756, January 1975.

2. C.K. Zoltani, Evaluation of the computer codes, BLAST, DORF,

References

HELP and HEMP for suitability of underexpanded jet flow calcula-
tions, BRL Report R1659, August 1973.

3. G.R. Moore, Finite difference calculations of the free-air
gun blast about the muzzle of a 5"/54 naval gun, NWL Technical
Report TR-2794, September 1972.

4. F.H. Maillie, Numerical calculation of a 105mm gun blast with
projectile, NWL Technical Report TR-3002, August 1973.

5. G.R. Moore, F.H. Maillie, G. Soo Hoo, Calculation of 5"/54
muzzle blast and post ejection environment on projectile, NWL
Technical Report TR-3000, January 1974.

6. G. Soo Hoo, Finite difference calculations of the free-air
blast field for an 8"/36 gun, NWL Technical Report TR-3122, June
1974.

7. R.M. Traci, J.L. Farr, C.Y. Lin, A numerical method for the
simulation of muzzle gas flows with fixed and moving boundaries,
BRL Contract Report CR-161, June 1974.

8. D.R. Ausherman, Muzzle blast flow field analysis for an M16
rifle, BRL Contract Report CR-196, December 1974.

9. C.W. Nelson, Numerical calculation of flow from recoilless
rifle nozzle, BRL Report 1688, 1973.

10. M. Rich, A method for Eulerian fluid dynamics, Los Alamos
Scientific Lab. Report LAMS-2826, December 1962.

11. R.A. Gentry, R.E. Martin and B.J. Daly, An Eulerian dif-
ferencing method for unsteady compressible flow problems, J.
Comp. Phys. 1, 87, 1966.

12. F.H. Harlow, Two-dimensional hydrodynamic calculations, Los
Alamos Scientific Lab. Report LA-2301, April 1959.

13. G. Moretti, Importance of boundary conditions in the numeri-
cal treatment of hyperbolic equations, Phys. of Fl. 12, 12, 1969.

References

14. C.K. Zoltani, The intermediate ballistic environment of the M16 rifle, BRL Report 1860, 1976

15. G. Moretti, The λ-scheme, Comp. and Fl. 7, 191, 1979.

16. T. de Neef and G. Moretti, Shock fitting for everybody, to appear in Comp. and Fluids.

17. G. Moretti, Numerical integration of compressible, viscous flow equations, POLY M/AE Rep. No. 79-40, 1979.

18. G. Moretti, Muzzle blast flow and related problems, AIAA Paper 78-1190, 1978.

19. F.H. Oertel, Jr., Investigations of transitional ballistics in muzzle jet flow simulators, BRL Report 2686, 1976.

20. E.M. Schmidt and D.D. Shear, Optical measurements of muzzle blast, AIAA J. 13, 1086, 1975.

21. G. Klingenberg, Investigation of combustion phenomena associated with the flow of hot propellant gases, Comb. and Flame 29, 289, 1977.

REPORT DOCUMENTATION PAGE		READ INSTRUCTIONS BEFORE COMPLETING FORM
1. REPORT NUMBER POLY-M/AE Report No. 80-10	2. GOVT ACCESSION NO. AD-HC87 597	3. RECIPIENT'S CATALOG NUMBER
4. TITLE (and Subtitle) A Numerical Analysis of Muzzle Blast-Precursor Flow		5. TYPE OF REPORT & PERIOD COVERED FINAL 1 JAN 77 — 30 JUN 80
		6. PERFORMING ORG. REPORT NUMBER
7. AUTHOR(s) Gino Moretti		8. CONTRACT OR GRANT NUMBER(s) DAAG 29-77-G-0072
9. PERFORMING ORGANIZATION NAME AND ADDRESS Polytechnic Institute of New York Route 110 Farmingdale, New York 11735		10. PROGRAM ELEMENT, PROJECT, TASK AREA & WORK UNIT NUMBERS Project No. P14369-E
11. CONTROLLING OFFICE NAME AND ADDRESS James J. Murray U. S. Army Research Office Research Triangle Park, NC 27709		12. REPORT DATE May 1980
		13. NUMBER OF PAGES 59
14. MONITORING AGENCY NAME & ADDRESS(if different from Controlling Office)		15. SECURITY CLASS. (of this report) Unclassified
		15a. DECLASSIFICATION DOWNGRADING SCHEDULE

16. DISTRIBUTION STATEMENT (of this Report)

Approved for public release; distribution unlimited.

17. DISTRIBUTION STATEMENT (of the abstract entered in Block 20, if different from Report)

NA

19. KEY WORDS (Continue on reverse side if necessary and identify by block number)

Muzzle blast, compressible flow, unsteady flow, viscous flow numerical gas dynamics

LAMBDA

20. ABSTRACT (Continue on reverse side if necessary and identify by block number)
The precursor flow evolution in a muzzle blast is simulated by a numerical analysis of a compressible, viscous, unsteady flow. Main features of the analysis are: use of a computational grid obtained by conformal mapping, the λ-scheme for integration of the Navier-Stokes equations, simplified treatment of shocks and boundary points. After a discussion of separation effects on a divergent channel, applications are made to the firing of a bullet. The calculation is continued until the bullet is completely out of—

DD FORM 1473
1 JAN 73

Cont'd

Unclassified

SECURITY CLASSIFICATION OF THIS PAGE (When Data Entered)

20.   Abstract - Continued

the barrel.   The mesh used has 16x16 intervals; despite its
coarseness, the details are remarkably accurate.